Dynamic regulations of co-translational protein targeting by the Signal Recognition Particle Receptor in *E. coli* and human

Thesis by

Yu-Hsien Hwang-Fu

In Partial Fulfillment of the Requirements for
the degree of
Doctor of Philosophy

CALIFORNIA INSTITUTE OF TECHNOLOGY
Pasadena, California

2019
(Defended Dec 10, 2018)

Yu-Hsien Hwang-Fu
ORCID: 0000-0002-2861-4843

Acknowledgements

First, I would like to express my sincere gratitude to my advisor, Professor Shu-ou Shan, for her unreserved guidance, support, and encouragement during my graduate studies. She has always been approachable whenever I need advice on any topics. Her passion and dedication in pursuing the truth of nature have deeply inspired me. It is a great honor to have been trained by her as a scientist.

I am grateful to my thesis committee, Professor William 'Bil' Clemons, Professor Thomas Miller, and Professor Carl Parker, for their supportive comments and suggestions about my projects and career path. In addition, I would like to acknowledge my undergraduate mentors who supported me in my pursuit of research: Professor Yuan-Chung Cheng and Professor Chun Chung 'Jerry' Chan.

I treasure the opportunity of working in the inspirational and warm Shan lab community. This group of people is tightly bound to each other while enjoying the sciences that they share on daily basis. Thank you to David Akopian, Aileen Ariosa, Sowmya Chandrasekar, Un Seng Chio, Hyun Ju Cho, Hao-Hsuan Hsieh, Jae Ho Lee, George Liang, Camille McAvoy, Thang Nguyen, Meera Rao, Michael Rome, Kuang Shen, Alex Siegel, Shuai Wang, and Chien-I Yang. All together, they have provided me the most collaborative and stimulatory environment that I could have ever asked for.

Special thanks to the mammalian SRP team: Sowmya Chandrasekar, Jae Ho Lee, and Hao-Hsuan Hsieh. The enormous mammalian SRP projects would have been an impossible challenge without the best collaborators. I am privileged to have

joined the team in the third year of my graduate studies and very honored to have worked closely with these brilliant people. Sowmya and Jae Ho have especially contributed a great amount of work to the third chapter of this thesis.

I gave another special thanks to Kuang Shen for his mentorship at the beginning of my studies at Caltech, as well as for the lasting friendship over the years. He has trained me in the basic biochemistry techniques that became an important foundation for my current experimental skills.

I am also grateful for the wonderful collaborators outside of the Shan lab. I thank Professor Jay Groves from UC Berkeley and his student William YC Huang for their generous help in the technique transplant of supported lipid bilayer. I thank Professor Thomas Miller for his guidance on data analysis of the single-molecule experiments. I thank Professor Robert Phillips and his student Tal Einav for the sparkling discussion about the physical insight of our discovery. I thank Dr. Heun Jin Lee from the Phillips lab for generously sharing his knowledge and offering help on many issues I had with microscopy instrumentations.

I could not have finished my graduate work without the support of my friends. I cherish the friendships I have built at Caltech with Sowmya Chandrasekar, Un Seng Chio, Jae Ho Lee, Chien-I Yang, Hyun Gi Yun, and Albert Chern. I also thank my roommates Ho-Hsuan Wei and Chia-Wei Hsu for making our place a warm home where I could seek rest and comfort.

I thank my parents for their unconditional love and their encouragement. Finally, I would like to thank my partner, Chi-wei Tseng, for his love and support throughout the journey of life.

Abstract

The Signal Recognition Particle (SRP) and its receptor (SR) co-translationally deliver the majority of secretory and membrane proteins to their membrane destinations. SRP recognizes and binds to the cargo, and SR recruits the transit complex to the target membrane. Precise timing and coordination are encoded into the interactions between SRP and SR in response to the cargo and environment to enable efficient and accurate targeting. This dissertation explores the regulation mechanisms of SRP membrane recruitment by SR in both bacteria and eukaryotes.

The bacterial SR is a peripheral membrane protein and recruits SRP by adjusting its membrane-binding modes. A complete kinetic model of SRP membrane recruitment by the SR was established based on direct observations and quantitative analyses of protein-membrane binding events at single-molecule resolution. Biochemical and cell biological examinations validated the physiological significance of the newly discovered dynamic membrane-binding mode of the SR. The two-stage SR membrane binding mechanism ensures both speed and specificity in bacterial co-translational protein targeting.

In eukaryotes, a proper initial recognition of SRP sets the right course for membrane delivery of the transit complex, as eukaryotic SR is anchored on the endoplasmic reticulum. A Molecular Recognition Feature (MoRF) in the disordered linker domain of eukaryotic SR was identified and characterized. The SR MoRF element enables rapid SRP-SR assembly in response to the ribosomal content of the cargo. The stimulation by SR MoRF is only present in eukaryotes and is likely a functional replacement of the tetraloop in bacterial SRP RNA whose stimulatory role was abolished during evolution.

Published Content and Contributions

Hwang Fu Y.H., Huang W.Y.C., Shen K., Groves J.T., Miller T., and Shan S.-O. (2017). "Two-step membrane binding by the bacterial SRP receptor enables efficient and accurate co-translational protein targeting." In: *eLife* **6**, e25885. doi: 10.7554/eLife.25885

Y.H.H.F. participated in the conception of the project, designed experiments, conducted experiments, and participated in the writing of the manuscript.

Hwang Fu Y.H., Chandrasekar S., and Shan S.-O. (2019). "A Molecular Recognition Feature mediates ribosome-induced SRP and SRP receptor assembly during co-translational protein targeting." *Submitted.*

Y.H.H.F. participated in the conception of the project, designed experiments, conducted experiments, and participated in the writing of the manuscript.

Table of Contents

Chapter 1: Introduction

Accurate localization, folding, and maturation of newly synthesized proteins are essential to all lives. The co-translational protein targeting pathway, composed of the Signal Recognition Particle (SRP) and its receptor, targets ~95% of the secretory and membrane proteins to the endoplasmic reticulum or the plasma membrane in bacteria (Walter & Johnson 1994; Akopian, Shen, et al. 2013). As these nascent proteins can properly fold only at their cellular destinations, their transportation across the aqueous cytosol poses a special challenge to the cell. The SRP pathway took an elegant strategy by coordinating targeting with translation, known as "co-translational protein targeting". A schematic diagram of bacterial SRP targeting process is depicted in Figure 1.1. SRP recognizes and binds to the translating ribosome as soon as the signal peptide or the first transmembrane segment emerges from the ribosome exit tunnel (Figure 1.1 step 1). This form of translating ribosome is often referred to as Ribosome-Nascent chain Complex, RNC. The SRP receptor, SR, brings the RNC-loaded SRP to the membrane by forming a complex with SRP (Figure 1.1 step 2). The SRP-SR complex then unloads the RNC to the translocation machinery (Figure 1.1 step 3), where the nascent proteins are translocated across or integrated into the membrane (Figure 1.1 step 4). A high level of spatial and temporal accuracy is required at every step in SRP pathway, making it an important system for studying how biology builds order from seemingly chaotic chemical soup.

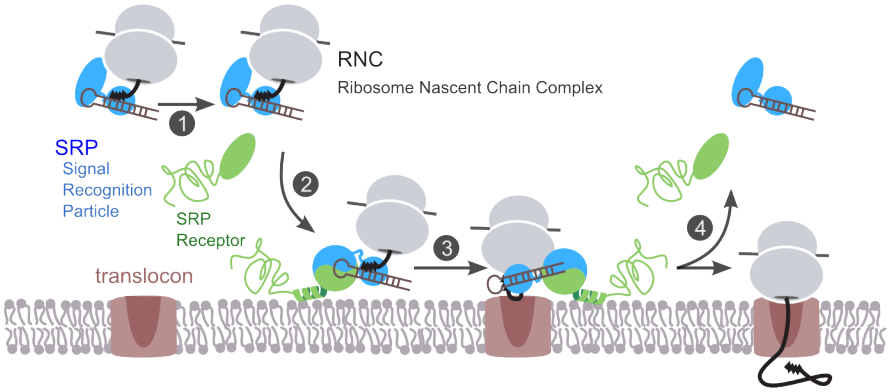

Figure 1.1

Co-translation protein targeting by SRP and SR. Step 1: RNC-recognition by SRP. Step 2: Membrane recruitment of SRP-RNC transit complex by SR. Step 3: Cargo unloading onto translocon through a conformation activation of the SRP-SR complex. Step 4: Nascent protein is translocated across the membrane, while SRP and SR dissociate to enter a new round of targeting reaction. This schematic is based on bacterial SRP system.

Most of current understanding of SRP pathway is based on decades of studies on the bacterial SRP. SRP is an ancient ribonucleoprotein of an SRP54 (called Ffh in bacteria) protein bound to a 4.5S RNA. Bacterial SR, also called FtsY, is a peripheral membrane protein (Figure 1.2 Bacterial SRP). The universally conserved SRP54 contains a methionine-rich M-domain that binds to the RNA and the signal sequence of the nascent peptide on RNC, and a NG-domain that dimerizes with the homologous NG-domain in FtsY. The NG-domains in SRP54 and FtsY are a special class of GTPases of which the GTP hydrolysis activities are reciprocally regulated through dimerization. The conformation rearrangements are tightly

controlled by the GTPase cycle of the NG-domain dimer during the targeting reaction (Shan 2016). Results from extensive studies have achieved unprecedented resolution in the molecular details of the bacteria SRP-SR GTPase dimer and their regulating mechanisms (Zhang & Shan 2014). This rich information has set the ground for approaching more challenging questions. Two open fields regarding the SRP pathways are (1) molecular details of events at the membrane and (2) SRP machineries in higher eukaryotes. This dissertation aims to explore both aspects with a central focus on the roles of SRP receptor in regulating dynamic processes in protein targeting.

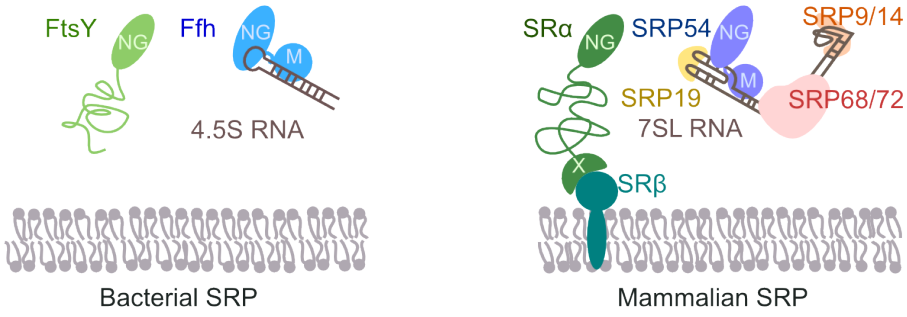

Figure 1.2

Compare bacterial (left) and mammalian (right) SRP and SR. The bacterial SRP54 and SR proteins are also called FtsY and Ffh, respectively. The disordered domains of FtsY and mammalian SRα are shown in wiggly lines.

We first address the membrane recruitment mechanism of the bacterial SRP pathway in chapter 2. For decades, FtsY has been considered to be in an activated conformation when on membrane for rapidly receiving cargo-loaded SRP (de Leeuw et al. 2000; Parlitz et al. 2007). However, this model forbids cargo

selectivity, as former studies showed that membrane-activated FtsY readily forms complex with SRP even without an RNC (Lam et al. 2010). To address this issue, we developed a fluorescence-based single-molecule microscopy to directly observe FtsY binding to supported lipid bilayer, which mimics membrane environment. We extracted the diffusion trajectories of individual membrane-bound FtsY from imaging data, where we built the first quantitative model of FtsY-membrane interaction. Surprisingly, we found that FtsY has two kinetically distinct membrane-binding modes: a dynamic and a stable mode. The stable mode corresponds to the known membrane-activated conformation of FtsY. We further connected the two binding modes to different stages in the targeting pathway and found that the dynamic mode corresponds to an intermediate conformation of the SRP and FtsY complex, where SRPs carrying wrong cargos are rejected.

Based on this discovery, we proposed a novel two-step model for the membrane recruitment mechanism in the SRP pathway: FtsY mostly interacts with the membrane in the dynamic mode that enforces cargo selectivity. Once it passes the selection checkpoint, FtsY rapidly transforms into the stable mode, which tightly binds cargo-loaded SRP and primes the targeting complex for downstream steps including cargo unloading and translocation. Our model provides an excellent example with molecular details of how specificity and speed are balanced in a cellular pathway, a fundamental challenge always faced by biological machineries.

In Chapter 3, we further explore the roles of mammalian SR at the early stage of the targeting pathway and its relating insights on the evolution from bacteria to

eukaryotes. Despite being discovered almost forty years ago, studies on the mammalian SRP machineries have been scarce due to the technical challenges accompanied the complexity of the system (Walter & Blobel 1980; Meyer & Dobberstein 1980). Eukaryotic SRP has expanded to a much larger 7SL RNA bound with the SRP54 protein and five additional protein subunits: SRP19, SRP68/72, and SRP9/14 (Figure 2.2 Mammalian SRP). Mammalian SR is an obligate complex composed of the SRα and SRβ subunits. SRβ subunit is a single-span transmembrane protein anchored at the endoplasmic reticulum. SRα tightly attached to SRβ through its N-terminal X-domain, followed by a 200-residue long disordered linker, and then is the conserved NG-domain (Figure 2.2 Mammalian SRP). Full *in vitro* reconstitution of mammalian SRP system has only been achieved recently by Lee et al (Lee et al. 2018). This breakthrough opened many possibilities in studying the molecular mechanisms of mammalian SRP machineries.

We identified and characterized a Molecular Recognition Feature (MoRF) element in the disordered linker of mammalian SR (Mohan et al. 2006). Deleting or mutating this motif in the linker severely impacts the SRP-SR assembly rate and targeting function. Through rigorous kinetic studies, we showed that SR MoRF plays a crucial role in mediating accelerated complex formation between SRP and SRα in response to the ribosomal component in the RNC. The functional roles and kinetic features of SR MoRF element are reminiscent of those of 4.5S RNA in the bacterial SRP, where the RNA stimulates SRP-SR assembly in response to RNC

through forming a transient charge tether between the GNRA tetraloop and the FtsY NG-domain. Interestingly, in the meanwhile, we found that mammalian SRP has lost the sensitivity to mutations in the RNA tetraloop that are detrimental to bacterial SRP-FtsY assembly (Zhang et al. 2008; Shen & Shan 2010). Putting together these observations, we proposed that the function of bacterial SRP RNA has migrated to the SR Linker domain during evolution.

From bacteria to mammals, the SRP pathway never ceases surprising us with its intricate designs for accuracy and efficiency in targeting nascent proteins. The SRP receptor, located at the critical junction where the targeting pathway switches from cytosol to membrane environment, serves a special role in mediating the dynamic interactions among cytosolic and membrane factors. The bacterial SR actively participates substrate selection and transforms into the committed form delivering correct cargos to the membrane. The eukaryotic SR exploits the MoRF element in its intrinsically disordered linker to sense ribosome and turns on rapid complex assembly with SRP. The work in this dissertation uncovers basic principles underlying complicated protein machineries and contributes to understanding of how organizations and functions are built in cells.

Chapter 2: Two-Step Membrane Binding by the Bacterial SRP Receptor Enable Efficient and Accurate Co-Translational Protein Targeting

A version of this chapter was first published as: Hwang Fu Y.H., Huang W.Y.C., Shen K., Groves J.T., Miller T., and Shan S.-O. (2017). "Two-step membrane binding by the bacterial SRP receptor enables efficient and accurate co-translational protein targeting." In: *eLife* **6**, e25885. doi: 10.7554/eLife.25885

ABSTRACT

The signal recognition particle (SRP) delivers ~30% of the proteome to the eukaryotic endoplasmic reticulum, or the bacterial plasma membrane. The precise mechanism by which the bacterial SRP receptor, FtsY, interacts with and is regulated at the target membrane remain unclear. Here, quantitative analysis of FtsY-lipid interactions at single-molecule resolution revealed a two-step mechanism in which FtsY initially contacts membrane via a Dynamic mode, followed by an SRP-induced conformational transition to a Stable mode that activates FtsY for downstream steps. Importantly, mutational analyses revealed extensive auto-inhibitory mechanisms that prevent free FtsY from engaging membrane in the Stable mode; an engineered FtsY pre-organized into the Stable mode led to indiscriminate targeting *in vitro* and disrupted FtsY function *in vivo.* Our results show that the two-step lipid-binding mechanism uncouples the membrane association of FtsY from its conformational activation, thus optimizing the balance between the efficiency and fidelity of co-translational protein targeting.

INTRODUCTION

Co-translational targeting of nascent membrane and secretory proteins by the Signal Recognition Particle (SRP) is an essential and universally conserved pathway that mediates the proper localization of almost 30% of the proteins encoded by the genome. The universally conserved core of SRP contains an SRP54 protein (termed Ffh in bacteria) tightly bound to an SRP RNA. A methionine-rich M-domain in SRP54 (or Ffh) recognizes the signal sequences on nascent polypeptides emerging from translating ribosomes. The GTPase domain, termed NG-domain, in SRP54 (or Ffh) interacts with a highly homologous NG-domain in SR (termed FtsY in bacteria), thus delivering the ribosome-nascent chain complex (RNC) to the eukaryotic endoplasmic reticulum (ER) or the bacterial plasma membrane (Walter & Johnson 1994; Cross et al. 2009). At the membrane, the RNC is unloaded from the SRP•SR complex onto the Sec61p (or SecYEG) translocon, via which the nascent protein is either integrated into or translocated across the membrane.

Extensive work on the bacterial SRP showed that the delivery of RNCs to the target membrane is actively regulated by the substrate and translocon complex (Akopian, Shen, et al. 2013; Zhang & Shan 2014). During each targeting cycle, the SRP•FtsY complex sequentially transitions between three conformational states, *early*, *closed* and *activated*, that culminate in their reciprocal GTPase activation (Zhang et al. 2008; Zhang et al. 2009). The *early* complex is a GTP-independent labile intermediate that stably forms only when SRP is loaded with RNCs bearing

SRP-dependent substrate proteins (Zhang et al. 2010; von Loeffelholz et al. 2013; Bradshaw et al. 2009). This stabilization enables the *early* intermediate to preferentially rearrange to the stable *closed* complex rather than dissociating, thus allowing rapid formation of the *closed* RNC•SRP•FtsY targeting complex at the membrane. Finally, the SecYEG complex drives additional NG-domain rearrangements that are coupled to GTPase activation and unloading of the RNC onto the translocon (Shen et al. 2012; Akopian, Dalal, et al. 2013; Ataide et al. 2011). These substrate- and translocon-driven conformational changes of the SRP•FtsY complex ensure productive targeting of the correct SRP substrates, while also providing key mechanisms to reject SRP-independent proteins from the pathway (Figure 2.1).

Compared to the RNC, the interaction of FtsY with phospholipid membranes and the role of membrane in the targeting reaction remain incompletely understood. FtsY has a poorly conserved acidic A-domain preceding its NG-domain. The A-domain has been implicated in interaction of FtsY with the membrane and translocon, but its precise roles remain unclear (de Leeuw et al. 2000; Angelini et al. 2005; Angelini et al. 2006; Weiche et al. 2008; Braig et al. 2009; Kuhn et al. 2015). Most previous work has focused on an amphiphilic lipid binding helix, here termed αN1, at the junction between A- and NG-domains. These studies showed that while the FtsY NG-domain itself could not stably bind membrane nor support efficient protein targeting, inclusion of Phe196 from the A-domain stabilizes the

helical structure of αN1 and restores both activities in the FtsY-NG+1 construct (Parlitz et al. 2007; Lam et al. 2010; Stjepanovic et al. 2011).

Importantly, lipid interaction via αN1 strongly stimulates FtsY's GTPase activity and formation of the *closed* SRP•FtsY complex (Lam et al. 2010; Stjepanovic et al. 2011). This is because in free FtsY, αN1 tightly packs against the remainder of the N-domain and sterically occludes approach of Ffh (Neher et al. 2008; Draycheva et al. 2016). Multiple observations suggest that lipid interaction of αN1 removes it from these auto-inhibitory contacts and thus primes FtsY for complex formation with SRP: (i) αN1 was proteolytically cleaved in all the crystal structures of *closed* SRP•FtsY complexes (Shepotinovskaya & Freymann 2002; Gawronski-Salerno & Freymann 2007; Shepotinovskaya et al. 2003; Egea et al. 2004; Focia et al. 2004); (ii) EPR studies showed that formation of the *closed* complex with SRP leads to significant mobilization of the αN1 helix, suggesting that it is released from the remainder of FtsY (Lam et al. 2010); (iii) consistent with the prediction from (ii), closed complex formation with SRP substantially increases the binding of FtsY to liposomes (Lam et al. 2010; Parlitz et al. 2007); and (iv) an FtsY-dN1 mutant, in which αN1 is deleted, is superactive in GTPase activity and in stable complex formation with SRP (Neher et al. 2008), phenocopying the stimulatory effect of lipids on FtsY. Together with the finding that lipids are also required for the interaction of FtsY with the SecYEG translocon (Kuhn et al. 2015), these observations led to the current model in which most FtsY molecules are membrane-bound through the αN1 helix and pre-activated for receiving cargo-

loaded SRP (Kuhn et al. 2015; Parlitz et al. 2007; Lam et al. 2010; Draycheva et al. 2016; Braig et al. 2011) (Figure 2.1, lower pathway in *blue*).

Nevertheless, rigorous formulation and consideration of this model lead to a number of conceptual conundrums. During SRP-dependent targeting, substrate-driven assembly of the SRP•FtsY *closed* complex is the major fidelity checkpoint at which incorrect SRP substrates are rejected, as they mediate this assembly up to 10^3-fold more slowly than the correct substrates (Zhang et al. 2010). However, liposome-activated FtsY rapidly forms a closed complex with SRP even in the absence of the RNC (Lam et al. 2010). Thus, if the pathway occurs primarily through pre-activated FtsY at the membrane according to the current model (Figure 2.1, lower route in *blue*), this would potentially bypass an important selection mechanism in the SRP pathway. The alternative path, in which FtsY assembles a *closed* complex with SRP in the cytosol and then interacts with the membrane (Figure 2.1, upper route in *magenta*), would preserve the specificity of substrate selection, but the unfavorable pre-equilibrium for FtsY's membrane interaction and activation could render the pathway less efficient. These considerations delineate a common challenge that biological pathways face in the trade-off between efficiency and specificity; how the SRP pathway overcomes this challenge is unclear.

Indeed, many observations suggest that the lipid interaction of FtsY is more complex than depicted in the current model. The notion that FtsY contains multiple membrane binding motifs was initially suggested by the observation that FtsY induces extensive liposome aggregation, implying a single FtsY interacting with

multiple membranes (de Leeuw et al. 2000). Later, the extreme N-terminus of the A-domain was identified as a secondary lipid binding motif based on sequence conservation and its ability to confer carbonate-resistant membrane association of FtsY (Weiche et al. 2008; Braig et al. 2009). However, the function of the additional membrane-binding motif(s) in FtsY and its relationship with the αN1 motif remain unclear.

To address these issues, we carried out the first quantitative analysis of FtsY's membrane interaction using single-molecule fluorescence microscopy on supported lipid bilayers. The sensitivity and resolution of this assay allowed us to detect two distinct modes of membrane interactions: a Dynamic mode mediated by the extreme N-terminus of the A-domain, and a Stable mode mediated by the αN1 motif. Free FtsY is auto-inhibited and interacts with the membrane primarily in the Dynamic mode. A conformational change is required for FtsY to engage the membrane in the Stable mode, which is driven by complex assembly with SRP. An engineered FtsY pre-organized into the Stable mode led to indiscriminate targeting *in vitro* and was unable to support cell growth *in vivo.* These results lead to a new model in which the Dynamic mode allows the membrane association of FtsY to be uncoupled from its conformational activation at the membrane, thus ensuring both the efficiency and fidelity of the targeting pathway.

RESULTS

SRP induces a switch in the membrane interaction mode of FtsY

To rigorously investigate FtsY-membrane interactions at high resolution, we assembled supported lipid bilayers (SLB) on microscope coverslips (Lin et al. 2010; Cremer & Boxer 1999; Seu et al. 2007). Total internal reflection fluorescence (TIRF) microscopy allowed us to directly observe membrane association events of fluorescently labeled FtsY on the SLB at single-molecule resolution (Figure 2.2A). Since TIRF illumination excites ~100 nm above the focal surface, the association and dissociation of individual FtsY molecules to and from the SLB were monitored by the appearance and disappearance, respectively, of quantized, discrete fluorescent spots. Time trajectories for the appearance, movement, and disappearance of individual fluorescent spots on SLB were constructed using an established particle-tracking routine (see Materials and Methods). Representative trajectories are shown in Figures 2.2B–D.

We observed two types of trajectories that represent FtsY molecules interacting with the membrane in distinct modes. With free FtsY, most of the molecules associated with and dissociated from SLB rapidly, while a small fraction of molecules stably associated with and diffused two-dimensionally on the SLB (Figure 2.2B). Importantly, when FtsY assembles a stable complex with SRP in the presence of the non-hydrolyzable GTP analog GppNHp (5'-Guanylyl imidodiphosphate), most of the SRP•FtsY complexes stably bound to membrane, while a small fraction of the complex exhibited rapid association and dissociation

on the SLB (Figure 2.2C). Few fluorescence spots were detected on the SLB with a negative control FtsY-dN1, in which all the potential membrane interacting motifs in FtsY were deleted (see Introduction and Figure 2.5 below), indicating low false-positive signals from free dye or background noise (Figure 2.2D).

To quantify the dissociation rate constants of FtsY from SLB, we calculated the Survival Probability Distribution, $P_{survival}(t)$, for all the trajectories under each condition. $P_{survival}(t)$ is defined as the probability that individual particles remain on the SLB for another time interval t, given that the particle is initially on the SLB (see Materials and Methods). The $P_{survival}(t)$ curves in the absence and presence of SRP were both bi-phasic and fit well to the sum of two exponential functions with dissociation rate constants of $k_{-1} = 14\ s^{-1}$ and $k_{-2} = 0.081\ s^{-1}$ (Figures 2.2E & F), whereas single exponential functions do not adequately fit the data (Figure 2.2-Figure supplement 1). This corroborates the presence of two populations of FtsY or SRP•FtsY complexes that interact with the membrane with distinct kinetic stabilities. The rate constants for individual populations are the same, within experimental error, for free FtsY and the SRP•FtsY complex (Figure 2.2F). While >90% of free FtsY are in the rapidly-dissociating population, the slowly-dissociating population dominates the SRP•FtsY complex (Figures 2.2F & G, P_1 and P_2).

These data support a model in which FtsY samples two conformations that interact with the membrane in distinct modes, termed the ‘Dynamic’ and ‘Stable’ modes for the rapidly- and slowly-dissociating populations, respectively, and SRP

binding shifts the conformational equilibrium of FtsY towards the Stable mode (Figure 2.3A & B). Although more complex models can be invoked, there was no evidence for additional conformational states of FtsY that affect its membrane interaction; thus, Figure 2.3 depicts the simplest model that accounts for all the SLB data in this study. The remainder of the rate and equilibrium constants in this model were determined or calculated as follows.

To analyze the kinetics of FtsY association with SLB, we quantified the cumulative appearances of new SLB-bound trajectories as a function of time (Figures 2.3C & D). As the lifetime of the trajectory on SLB (t) for the Dynamic mode is >100-fold shorter than the Stable mode, we used a cutoff of t = 0.25 seconds to distinguish trajectories in the Dynamic and Stable modes; use of this cutoff gave population quantifications that agreed well with the results from survival probability analysis (cf. Figure 2.3-Figure supplement versus Figure 2.2F, P_1 & P_2). Linear fits of the data gave the apparent association rate constant for molecules that bind the membrane in each mode (Figures 2.3C & D and Figure 2.3-Figure supplement, $k_{1,app}$ and $k_{2,app}$, respectively). These association rate constants are apparent, as the number of accumulated traces were normalized by the total concentration of FtsY or SRP•FtsY complex and did not take into account the fraction of molecules in each conformation in solution. Numerically solving the models in Figures 2.3A and B based on mass conservation and the measured kinetic parameters allowed us to extract true FtsY-membrane association rate constants in the Dynamic and Stable modes (Figure 2.3E, k_1 and k_2, respectively; see Materials

and Methods). The conformational equilibria between the Dynamic and Stable modes at the membrane (K_{mem}^{FtsY} and $K_{mem}^{\mathrm{SRP{\bullet}FtsY}}$ in Figures 2.3A & B, respectively) were directly obtained from the ratios of membrane-bound populations in the two modes (P_1 and P_2 in Figure 2.2F). The conformational equilibria in solution (K_{cyto}^{FtsY} and $K_{cyto}^{\mathrm{SRP{\bullet}FtsY}}$) were calculated based on the measured kinetic parameters and thermodynamic coupling of the conformational equilibria to the equilibria of FtsY-membrane interactions (see Materials and Methods).

Inspection of the parameters in this model yielded three interesting observations. First, FtsY-membrane association is ~10-fold slower in the Stable than the Dynamic mode (Figure 2.3E, k_1 / k_2). Second, SRP drives the conformational equilibrium of FtsY to the Stable mode ~130 fold ($K_{cyto}^{\mathrm{SRP{\bullet}FtsY}}$ / K_{cyto}^{FtsY} and $K_{mem}^{\mathrm{SRP{\bullet}FtsY}}$ / K_{mem}^{FtsY}). Finally, the Dynamic-to-Stable transition of FtsY is favored at least 14-fold at the membrane (K_{mem} / K_{cyto}). Together, these observations provide the first quantitative evidence for a regulatory switch at FtsY's membrane recruitment step, during which FtsY tunes its membrane interactions in response to SRP.

To identify the conformational change responsible for the SRP-induced switch of FtsY from the Dynamic to the Stable mode, we used a previously characterized set of mutant GTPases or GTP analogues that stall the SRP•FtsY complex at distinct conformational stages. Omission of *nucleotide* or mutant FtsY(G455W) inhibits the *early*-to-*closed* rearrangement, and thus locks the SRP•FtsY complex at the *early* intermediate stage (Figure 2.4A, (Zhang et al.

2008)). Mutant FtsY(A335W) inhibits active site rearrangements that lead to GTPase activation, and thus locks the SRP•FtsY complex in the *closed* state (Figure 2.4A, (Shan et al. 2004)). We tested the membrane-binding abilities of SRP•FtsY complexes assembled with these mutants or nucleotide analogues using the SLB-smTIRF setup. As excess FtsY was needed to drive formation of the *early* complex, we labeled SRP instead of FtsY in these experiments to remove contributions from free FtsY. SRP•FtsY(A335W) displayed comparable amounts of Stable SLB interactions as the wildtype complex (Figure 2.4B). In contrast, both conditions that stall the SRP•FtsY complex in the *early* conformational state significantly reduced the Stable mode of lipid interaction (Figure 2.4C). Thus, FtsY switches to the Stable mode during the *early*-to-*closed* rearrangement in the SRP•FtsY complex.

Together, the results in this section show that FtsY interacts with the membrane in two modes, a Dynamic and a Stable mode. While free FtsY predominantly interacts with the membrane in the Dynamic mode, complex formation with SRP drives most of FtsY into the Stable mode of interactions. The Dynamic-to-Stable switch occurs during the rearrangement of the SRP•FtsY complex from the *early* to the *closed* conformation.

Two functionally important motifs in FtsY mediate the Dynamic and Stable modes.

To define the sites responsible for FtsY's Dynamic and Stable interactions, we constructed a series of FtsY mutants in which individual motifs and domains of

FtsY are systematically truncated (Figure 2.5A). FtsY-d14 removes the N-terminal 14 residues of FtsY (termed the αA1 motif), which has been proposed as a secondary lipid binding motif (Weiche et al. 2008; Braig et al. 2009). FtsY-d46 removes a more substantial portion of the A-domain. FtsY-NG+1 and FtsY-NG contain the well-characterized αN1 helix, and the additional Phe196 in FtsY-NG+1 stabilizes this helix (Parlitz et al. 2007). Finally, FtsY-dN1 provides a negative control in which the entire A-domain and αN1 helix are deleted. Measurement of GTPase activity (Peluso et al. 2001) showed that in the absence of membrane, all of these mutants behave identically to full-length FtsY in association and reciprocal GTPase activation with SRP (Figure 2.5-Figure supplement 1 and (Powers & Walter 1997; Shan et al. 2007; Bahari et al. 2007)).

We measured the interactions of mutant FtsYs with SLB using smTIRF. Since the Dynamic and Stable modes dominate free FtsY and the SRP•FtsY complex, respectively, we tested these mutants under both conditions to dissect the contributions of potential binding motifs to each interaction mode. Representative trajectories are shown in Figure 2.5-Figure supplement 2. With free FtsY, removal of the αA1 motif (FtsY-d14) reduced interactions in the Dynamic mode >10-fold, and no substantial additional reductions were observed with further truncations (Figure 2.5B, solid bars). This indicates that the αA1 motif is primarily responsible for FtsY-lipid interactions in the Dynamic mode. In contrast, only complete truncation of the αN1 helix in FtsY-dN1 abolishes the Stable mode of interactions in the SRP•FtsY complex (Figure 2.5C, open bars), indicating that the αN1 motif

mediates the Stable mode. Thus, distinct motifs in FtsY mediate the Dynamic and Stable modes of lipid interactions.

To further probe the nature of the Dynamic mode, we tested the contribution of conserved basic residues in the αA1 motif (Lys3, Lys5, Lys6 and Arg7) (Figure 2.5D, (Weiche et al. 2008)); basic residues are enriched in αA1 and could mediate interaction with the anionic phospholipid headgroup (de Leeuw et al. 2000; Lam et al. 2010). To this end, we constructed FtsY mutants in which part or all of these charges are removed and/or reversed (Figure 2.5D, EE, EL, and EEEL). All these mutants exhibited two-fold reduced interactions with the membrane compared to wildtype FtsY in SLB-smTIRF measurements (Figure 2.5E). Nevertheless, the defects of these mutants are modest compared to FtsY-d14 (Figure 2.5E), suggesting that the aromatic and aliphatic residues in the remainder of αA1 also contribute to interaction in the Dynamic mode. Thus, the Dynamic mode is driven by a combination of electrostatic and hydrophobic interactions mediated by αA1.

Importantly, FtsY-d14 not only reduced the Dynamic mode, but also nearly abolished the Stable mode of interaction in free FtsY (Figure 2.5B & E), suggesting that interaction in the Dynamic mode is required to attain the Stable mode in free FtsY. Consistent with this notion, disruption of the Dynamic and Stable interactions are highly correlated in the αA1 charge mutants (Figure 2.5E). To independently test this model, we measured the lipid-mediated stimulation of FtsY's GTPase activity, which provides a readout for the conformational activation of FtsY upon engagement of the αN1 helix with the membrane (Lam et al. 2010). The GTPase

activity of wildtype FtsY is strongly stimulated by PG/PE liposomes as previously observed, whereas this stimulation was abolished in FtsY-d14, similar to the behavior of FtsY-NG (Figure 2.5-Figure supplement 3). Together, these results strongly suggest that in free FtsY, the Dynamic mode is upstream of and required for this receptor to further engage the membrane in the Stable mode.

To assess the contribution of the Dynamic interactions to biological function, we tested the ability of FtsY mutants to mediate the co-translational targeting and translocation of a model SRP substrate, preprolactin (pPL), into ER microsomal membranes (see Materials and Methods; Figure 2.6-Figure supplement). Removal of the αA1 motif reduced targeting efficiency to less than 30% of wildtype level (Figure 2.6A, FtsY-d14), indicating that αA1 is important for protein targeting. The set of αA1 charge mutants of FtsY (Figure 2.5D) provided a more controlled assessment of the contribution of the Dynamic mode. All these mutants reduced the efficiency of pPL targeting and translocation (Figure 2.6A), and the targeting efficiency correlated well with the amount of Dynamic interactions displayed by each variant in this set of mutants (Figure 2.6B). These results provide strong evidence for an important role of the Dynamic interactions in protein targeting mediated by full-length FtsY.

Intriguingly, as the remainder of the A-domain was further truncated in d14, d46, and NG+1, the Stable mode of lipid interactions in free FtsY (Figure 2.5B, open bars) was gradually restored. This suggests that the A-domain prevents free FtsY from engaging with the membrane in the Stable mode (Figure 2.5F, red line

from A-domain). With FtsY-NG+1, in which the entire A-domain is removed except for Phe196, the Stable and Dynamic interactions were restored to ~80% and ~20% of that of full-length FtsY, respectively (Figure 2.5B). This suggests that when the inhibitory A-domain was removed, the αN1 helix could also mediate Dynamic interactions with the membrane, albeit less efficiently than the αA1 motif (Figure 2.5G, dashed green arrow). As αN1 also mediates the Stable interaction, transition from the Dynamic to the Stable mode is likely more efficient in FtsY-NG+1 than in full-length FtsY. Nevertheless, FtsY-NG+1 still interacts weakly with the membrane by itself and requires SRP binding to drive favorable interaction with the membrane (cf. Figure 2.5B vs. C). Thus, additional auto-inhibitory interactions, presumably from the remainder of the N-domain (Neher et al. 2008; Draycheva et al. 2016), are present to prevent free FtsY-NG+1 from engaging with the membrane in the Stable mode (Figure 2.5F & G, red lines from N-domain). Finally, protein targeting efficiency paralleled the restoration of the Stable mode in free FtsY across the A-domain truncation mutants (Figure 2.6C, D), consistent with the Stable mode being an obligatory species during targeting.

Collectively, the results in this section showed that the Dynamic and Stable modes are mediated primarily by the αA1 and αN1 motifs of FtsY, respectively (Figure 2.5F, cyan and blue arrows). Before association with SRP, lipid interaction via αA1 is required for wildtype FtsY to further engage the membrane via the αN1 helix. This requirement is due, in part, to the inhibitory effect from the remainder of the A-domain, whose highly acidic nature likely repels FtsY from the membrane.

The αA1 motif likely provides an initial membrane attachment to overcome this inhibition, enabling the subsequent Stable mode and efficient targeting (Figure 2.5F, green lines); this explains why αA1 can be bypassed by truncations of the A-domain (Figure 2.5G). Finally, regardless of the presence of the A-domain, free FtsY exists in an auto-inhibited state for interaction with the membrane via αN1, and interaction with SRP is the dominant mechanism to driving FtsY to the conformation that interacts with the membrane in the Stable mode (Figure 2.5F & G).

The SRP-induced transition of FtsY's membrane interaction mode is unlikely to be an artifact of the DOPC/DOPS composition of the SLB. First, bacterial SRP and FtsY can replace their mammalian homologues and mediate efficient targeting and insertion of mammalian substrates into ER microsomes (Powers & Walter 1997) with a similar substrate selection pattern (Zhang & Shan 2012). These observations indicate that the core regulatory mechanisms of SRP and the SRP receptor are insensitive to the difference in lipid composition between the bacterial plasma membrane and the mammalian ER membrane. Second, although FtsY exhibits a preference for PG, previously observed lipid-stimulation of FtsY's biochemical activities required liposomes containing 70-100% PG, whereas total *E. coli* lipids or liposome compositions that mimic the *E. coli* plasma membrane did not induce detectable stimulations of FtsY (de Leeuw et al. 2000; Lam et al. 2010; Stjepanovic et al. 2011). These earlier results agree well with our model, showing that the majority of FtsY is in the auto-inhibited state in its native lipid environment. Third,

we repeated the SLB measurements using DOPC/DOPG side-by-side with DOPC/DOPS (Figure 2.5-Figure supplement 4). No significant differences between SLBs generated from the different lipid compositions were observed, indicating that the identity of anionic phospholipids (PG in bacterial plasma membrane and PS in the ER membrane) does not impact FtsY's lipid interaction modes. Finally, the model derived from the SLB measurements were extensively tested by *in vitro* targeting assays using ER microsomes and *in vivo* complementation assays in bacteria (see the next section); the good agreement between the results of all three assays further suggests that modest variations in lipid composition does not alter the regulatory mechanism of SRP receptor shown here.

The Dynamic mode balances the specificity and efficiency of protein targeting.

The observation of extensive auto-inhibitory mechanisms for FtsY's membrane interaction raises a fundamental question: what is the role of these auto-inhibitory interactions? What is the penalty for evolving a receptor molecule that is pre-organized into the Stable mode on the membrane? A hypothesis stems from the consideration that FtsY-membrane interaction via αN1 is coupled to conformational activation of this receptor, which enables FtsY to pre-organize into the *closed* conformation and bind SRP much more rapidly (Neher et al. 2008). As discussed in the Introduction, formation of the *closed* SRP•FtsY complex is a major cargo selection step in the SRP pathway (Zhang et al. 2010; von Loeffelholz et al. 2013). FtsY molecules pre-organized into the Stable mode could potentially bypass this

key checkpoint and thereby compromise fidelity. In this context, the Dynamic mode provides a mechanism for FtsY to associate with the membrane without conformational activation, and thus preserves this fidelity checkpoint.

To test this hypothesis, we engineered an FtsY that bypasses the Dynamic mode and is pre-organized into the Stable mode. We used FtsY-dN1 to mimic the effect of lipids on pre-organizing FtsY into the *closed/activated* conformation. Multiple observations support the choice of this construct: (i) in apo-FtsY, the αN1 helix sterically occludes tight SRP•FtsY association in the *closed* conformation (Neher et al. 2008; Draycheva et al. 2016; Shepotinovskaya & Freymann 2002); (ii) lipid binding releases αN1 from the remainder of the protein and preorganizes FtsY into the *closed* state (Lam et al. 2010; Stjepanovic et al. 2011); (iii) as predicted from (i) and (ii), FtsY-dN1 phenocopies the effects of lipids on enhancing SRP•FtsY assembly and GTPase activation (Neher et al. 2008). Note that FtsY-NG+1 is not a proper construct to mimic a pre-organized FtsY, as free FtsY-NG+1 is still auto-inhibited and requires SRP to switch to the Stable mode (Figures 2.5B & C). To re-establish stable membrane association of FtsY, we tethered His_6-tagged FtsY-dN1 on the SLB doped with Ni-NTA-DGS lipids for *in vitro* assays (Figure 2.7B), or fused FtsY-dN1 to the spontaneous membrane-inserting 3L-Pf3 sequence (Figure 2.8A (Lim et al. 2013)) for *in vivo* assays.

To test whether the pre-organized FtsY can distinguish SRPs loaded with correct and incorrect cargos, we monitored the membrane targeting of RNC•SRP•FtsY complexes in the SLB-smTIRF setup (Figure 2.7). We presented

RNC•SRP complexes, labeled at SRP, to either wildtype (Figure 2.7A) or pre-organized FtsY (Figure 2.7B) and monitored the appearance of membrane-bound targeting complexes in real time. We tested RNCs bearing two representative nascent chains: FtsQ, a bona-fide SRP substrate, and Luc (luciferase), a cytosolic protein. Both wildtype and engineered FtsYs efficiently targeted RNC_{FtsQ} (Figure 2.7A & B, orange lines). However, while wildtype FtsY strongly rejected RNC_{Luc}, significant amounts of RNC_{Luc} were localized to the membrane by pre-organized FtsY-dN1 (Figure 2.7A & B, blue lines). We confirmed that the observed SRP-RNC_{FtsQ} targeting is dependent on FtsY (Figure 2.7-Figure supplement) . To more specifically test the role of conformational pre-organization in FtsY-dN1, we measured other FtsY A-domain truncation mutants (d14, NG+1, and NG) that showed SRP-dependent transition from the Dynamic to Stable mode. We tethered these mutants on SLB via Ni-His_6 interaction and compared the targeted SRP-RNC populations mediated by these constructs to those by FtsY-dN1 (Figures 2.7C & D). All these surface-tethered FtsY mutants mediated efficient targeting of RNC_{FtsQ}, but not RNC_{Luc}, to the SLB (Figure 2.7C, yellow vs. blue bars). Importantly, they all showed 5-10 fold more selective targeting than FtsY-dN1 (Figures 2.7 D). Thus, pre-organizing FtsY into the Stable mode compromises its ability to reject incorrect cargos bearing SRP-independent substrates.

To examine the consequence of pre-activating FtsY *in vivo*, we tested the ability of the pre-organized FtsY to complement FtsY depletion and support cell growth (Figure 2.8). TM-FtsYdN1 was expressed from the pTlac18 plasmid in *E.*

coli strain IY28, in which expression of chromosomal FtsY is under control of the *ara* promoter (Bahari et al. 2007). We tested cell growth on LB plates supplemented with either IPTG (Isopropyl β-D-1-thiogalactopyranoside) or L-arabinose after serial dilution of the culture. As controls, we also tested complementation by FtsY-d14, FtsY-NG and FtsY-NG+1 with or without N-terminal fusion to 3L-Pf3 (Figure 2.8). FtsY-NG+1 showed no significant defect in supporting cell growth, as described previously (Eitan & Bibi 2004; Bahari et al. 2007; Parlitz et al. 2007; Mircheva et al. 2009), whereas FtsY-d14 and FtsY-NG exhibited modest and strong defects, respectively (Figure 2.8 and Figure 2.8-Figure supplement). These results are consistent with the membrane binding and protein targeting activities of the respective mutants observed *in vitro*. Fusion to 3L-Pf3 rescued cell growth of both mutants FtsY-d14 and FtsY-NG (Figure 2.8 and Figure 2.8-Figure supplement), consistent with the robust RNC targeting activity of the corresponding tethered mutants observed in the SLB setup (Figure 2.7). This and cell fractionation analyses (Figure 2.8-Figure supplement) corroborated that the 3L-Pf3 sequence successfully restored the membrane localization of the mutant FtsYs. In contrast, FtsY-dN1 exhibited a strong defect in supporting cell growth that was not rescued by fusion to 3L-Pf3; this defect cannot be attributed to defects in the expression or localization of TM-dN1 (Figure 2.8 and Figure 2.8-Figure supplement). The fact that TM-NG was fully functional in supporting cell growth also ruled out possible folding defects of the NG-domain due to the 3L-Pf3 fusion. Most importantly, membrane-anchored FtsY-dN1 is highly efficient in targeting

correct SRP substrates (Figures 2.7B & C), indicating that deficient targeting was not responsible for the failure of TM-FtsYdN1 to support cell growth. Collectively, the combination of *in vitro* and *in vivo* data strongly suggest that pre-organizing FtsY into the Stable mode leads to promiscuous targeting that is detrimental to cells.

On the other hand, an unfavorable pre-equilibrium to reach the stable mode in free FtsY could compromise the efficiency of the pathway if FtsY only binds membrane via the Stable mode (Figure 2.1, upper path and Figure 2.9A). We assessed whether this presents a problem for protein targeting based on the rate constants in this targeting route. The rate constant for the *early*-to-*closed* (or Dynamic-to-Stable) rearrangement in solution (Figure 2.9A, k_{switch}^{cyto}) was determined to be 0.3–0.6 s^{-1} in previous studies and this work (Figure 2.9C), using acrylodan labeled at FtsY(C235) or FtsY(C356) (Zhang et al. 2009; Zhang et al. 2010; Akopian, Dalal, et al. 2013; Ariosa et al. 2013). These probes specifically change fluorescence upon rearrangement of the *early* SRP•FtsY intermediate to the *closed/activated* state (Zhang et al. 2009; Lam et al. 2010). The kinetics for interaction of the *closed* SRP•FtsY complex with the membrane via the Stable mode was determined above (Figure 2.3E, k_2 and k_{-2}). Kinetic simulations using these parameters showed that targeting via this route is <50% complete in 5 seconds (Figure 2.9D, magenta curve), whereas the entire SRP pathway must finish within 3-5 seconds in bacteria before the nascent chain reaches a critical length of ~130-140 amino acids (Noriega et al. 2014).

We asked whether, given this unfavorable conformational pre-equilibrium in free FtsY, the Dynamic mode enables a faster targeting route compared to a route that relies solely on the Stable mode (Figure 2.9B). This is probable, as in the route utilizing the Dynamic mode, the *early* complex can first associate with the membrane 10-fold more quickly (Figure 2.3E, $k_1 > k_2$). Using acrylodan-labeled FtsY(C356), we further found that lipids accelerated the rate constant of the *early*-to-*closed* rearrangement 25-fold (Figure 2.9C, $k_{switch}^{mem} > k_{switch}^{cyto}$). Kinetic simulations based on these rate constants demonstrated that the route using the Dynamic mode is five-fold faster than the alternative route (Figure 2.9D, blue curve). Thus, the Dynamic mode provides a kinetic advantage over alternative pathways that rely exclusively on the Stable mode, and alleviates the compromise in efficiency for FtsY molecules that are not pre-activated at the membrane.

DISCUSSION

In this work, quantitative analysis at single-molecule resolution revealed two distinct modes of membrane interactions of the bacterial SRP receptor FtsY. The Dynamic mode, characterized by rapid association with and dissociation from membrane (Figures 2.1-2.3), is primarily mediated by the αA1 motif (Figure 2.5). The Dynamic mode is required for FtsY to further engage with the membrane via the Stable mode, which is characterized by membrane association and dissociation kinetics 10-fold and 200-fold slower, respectively, than the Dynamic mode (Figures 2.1-3) and mediated by the previously characterized αN1 helix at the A-N domain junction (Figure 2.5). Importantly, while the Dynamic mode dominates in free FtsY and the *early* SRP•FtsY complex, the targeting complex switches to the Stable mode only when it forms the *closed* complex with SRP (Figure 2.4). These observations, together with additional findings here and previously (Parlitz et al. 2007; Lam et al. 2010; Neher et al. 2008; Shepotinovskaya & Freymann 2002), reveal extensive auto-inhibitory mechanisms for the FtsY-membrane interaction via αN1, in contrast to the currently accepted model in which targeting occurs through FtsY molecules that are pre-bound and activated at the membrane via the αN1 motif (Figure 2.1). An engineered FtsY pre-organized into the Stable mode compromises substrate selection by the targeting pathway *in vitro* (Figure 2.7) and disrupts FtsY function *in vivo* (Figure 2.8), suggesting that pre-activating FtsY at the membrane is associated with a severe penalty. We propose that the Dynamic mode, by providing an initial membrane attachment that is uncoupled from the conformational

activation of FtsY, ensures accurate substrate selection without significantly compromising the efficiency of the pathway.

Most previous work has focused on the αN1 helix of FtsY that mediates the Stable mode (Parlitz et al. 2007; Lam et al. 2010; Stjepanovic et al. 2011). Importantly, membrane interaction via αN1 also activates FtsY for interaction with SRP, rapid GTP hydrolysis, and subsequent cargo unloading onto the SecYEG complex (Shepotinovskaya & Freymann 2002; Gawronski-Salerno & Freymann 2007; Neher et al. 2008; Lam et al. 2010; Braig et al. 2011; Stjepanovic et al. 2011). This raises issues for the fidelity of substrate selection by SRP, as the kinetics of SRP-FtsY assembly is strongly regulated by the cargo and comprises a major substrate selection mechanism in the pathway (Figure 2.1, red arrows, (Zhang et al. 2010; von Loeffelholz et al. 2013)). In the extreme scenario where targeting occurs solely through FtsY molecules pre-activated at the membrane in the Stable mode prior to SRP binding, this important fidelity checkpoints would be bypassed (Figure 2.1, lower pathway). In support of this hypothesis, we found here that an engineered FtsY pre-organized into the Stable mode leads to indiscriminate targeting of SRP•FtsY complexes *in vitro* and cannot support cell growth *in vivo*. Thus, the fidelity of the SRP pathway demands that FtsY is not predominantly in the Stable/*closed* conformation before it encounters cargo-loaded SRP. Consistent with these notions, the results here and from previous work (Lam et al. 2010; Stjepanovic et al. 2011; Neher et al. 2008; Draycheva et al. 2016) show that free FtsY is extensively auto-inhibited for lipid interaction via αN1, and assembly of a

closed complex with SRP is required to drive FtsY molecules into the Stable mode. This auto-inhibition arises not only from the acidic A-domain as shown here (Figures 2.5 and 2.6) but also from the N-domain of FtsY, which forms tight intra-molecular interactions with αN1 in free FtsY that reduces its accessibility (Neher et al. 2008; Draycheva et al. 2016).

Auto-inhibitory mechanisms are often associated with a penalty in efficiency. The results here show that the Dynamic mode helps alleviate this penalty, by providing a targeting route that accelerates the formation of a stably membrane-bound targeting complex compared to routes that rely only on the Stable mode. This acceleration stems from two effects: (i) membrane interaction via the Dynamic mode is ~10-fold faster than the Stable mode (Figure 2.3); and (ii) once associated with the membrane in the Dynamic mode, the SRP•FtsY complex rearranges 25-fold more quickly into the Stable mode (Figure 2.9). More importantly, in contrast to the Stable mode, the Dynamic mode provides an initial membrane attachment without conformational activation of the receptor, and thus preserves important substrate selection mechanisms in this pathway.

We propose a revised model in which the two-step membrane binding mechanism of FtsY balances the trade-off between efficiency and selectivity (Figure 2.10). In this model, SRP initiates interaction with FtsY either in solution or bound to membrane in the Dynamic mode (Figure 2.10, events in yellow background); this generates the *early* targeting complex, which is strongly stabilized when SRP is loaded with a correct substrate (Zhang et al. 2009; Zhang et

al. 2010). Once the *early* complex localizes to the membrane in the Dynamic mode, phospholipids trigger its rapid and favorable rearrangement to the *closed* state, in which FtsY further uses the αN1 motif to engage the membrane in the Stable mode, and the complex is activated for interaction with and cargo unloading onto the SecYEG translocon (Figure 2.10, events in white background). In contrast to correct substrates, the SRP•FtsY early complexes formed with incorrect substrates are much less stable and can be rejected either in solution or when bound at the membrane in the Dynamic mode (Figure 2.10, red arrows).

It is important to note that the role of FtsY's Dynamic mode in preserving substrate selection derives from its ability to provide a membrane interaction mechanism that is uncoupled from FtsY's conformational activation. Thus, the dynamic nature of this interaction is not a prerequisite for receptor molecules in general. In principle, any membrane interaction mechanism that precedes and is uncoupled from activation of downstream events could fulfill this role. This explains why replacing the αA1 motif with the 3L-Pf3 TM (this work) or with another unrelated membrane protein (Zelazny et al. 2009) rescued the defects of FtsY mutants lacking the Dynamic mode, as long as the mutants are not conformationally pre-organized into the *closed* state. Also consistent with this model, fusing the more hydrophobic αA1 motifs from *S. lividans* FtsY to *E. coil* FtsY-NG rescued the activity of the latter (Bibi et al. 2001; Maeda et al. 2008). It is tempting to speculate that in eukaryotic cells, although the SRP receptor is anchored at the ER membrane via the transmembrane domain of the SRβ subunit, a

conceptually analogous switch in the conformation, activity, or interaction mode could be built into the eukaryotic SRP receptor (Miller et al. 1995).

In addition to phospholipids, the SecYEG translocon has been proposed to play a crucial role in FtsY's membrane localization and in receiving cargo-loaded SRP (Angelini et al. 2005; Angelini et al. 2006; Kuhn et al. 2015; Draycheva et al. 2016). A recent study also showed that phospholipids are required for FtsY-SecYEG association (Kuhn et al. 2015); this places the FtsY-SecYEG interaction downstream of the FtsY-membrane interactions described here (Figure 2.10). Additionally, FtsY exhibits a strong preference for anionic phospholipids, such as PG and cardiolipin, in the Stable mode (de Leeuw et al. 2000; Erez et al. 2010; Stjepanovic et al. 2011). The same preference has been found for SecYEG (Gold et al. 2010). These observations suggest that the SecYEG translocon could further enhance the transition of FtsY to the Stable mode and vice versa, either directly through induced conformational changes or indirectly through anionic phospholipids. These remain open possibilities for future studies.

Speed and accuracy define the competency of biological systems. How to balance the trade-off between these two parameters has been widely discussed, but in few systems has this concept been studied at molecular level (Hopfield 1974; Murugan et al. 2012). Much discussions have focused on transcription and protein synthesis machineries (Thompson & Karim 1982; Johansson et al. 2008; Wohlgemuth et al. 2010; Johansson et al. 2012). Our work illustrates an analogous accuracy-speed tradeoff for receptor molecules. Previous models of protein

targeting based solely on FtsY's Stable mode of membrane interaction exemplify extreme cases in which either speed or specificity is compromised (Figure 2.1). The two-step membrane-binding mechanism of FtsY resolves this dilemma and balances the tradeoff between efficiency and fidelity (Figure 2.10). This new model, which is largely based on energetic and kinetic principles, may provide a conceptually generalizable mechanism for membrane recruitment events in other receptor systems and targeting pathways.

MATERIALS AND METHODS

Vector, protein and RNA preparations. Plasmids for mutant FtsY were constructed using the QuikChange mutagenesis protocol (Stratagene). The expression construct for His_6-FtsY-dN1 was a kind gift from the Schaffitzel Lab. mRNAs for *in vitro* translations were synthesized by *in vitro* transcription using T7 (for RNC preparation) or SP6 (for co-translational translocation assay) polymerases following the Megascript protocol (Ambion). Wildtype/mutant Ffh and FtsY and 4.5S RNA were expressed and purified as described in previous studies (Peluso et al. 2001; Lam et al. 2010). RNCs bearing signal sequences of FtsQ or Luc were prepared as described previously (Zhang et al. 2010). FtsY-C345 and Ffh-C153 were labeled with Alexa647-maleimide (Invitrogen) and FtsY-C356 was labeled with acrylodan (Invitrogen) as described (Shen et al. 2012) with the minor modifications. Details see the SI Methods. All proteins were exchanged into SRP buffer (50 mM HEPES-KOH, pH 7.5, 150 mM KOAc, 10 mM $Mg(OAc)_2$, 2 mM dithiothreitol (DTT), and 0.01% octaethyleneglycol dodecylether (Nikkol)) prior to use.

Fluorescence Labeling. FtsY-C345 and Ffh-C153 were labeled with Alexa647-maleimide (Invitrogen) and FtsY-C356 was labeled with acrylodan (Invitrogen) as described (Shen et al. 2012) with the following modifications. The labeling reactions were carried out using 10-fold molar excess of Alexa647 and 30-fold molar excess of acrylodan over protein. Labeling reactions were carried out at 4°C for 2 and 16 hours for Alexa647 and acrylodan, respectively. The labeling

efficiencies of each sample were quantified using the following extinction coefficients of 270,000 $cm^{-1}M^{-1}$ and 16,400 $cm^{-1}M^{-1}$ for Alexa647 and acrylodan, respectively. Protein concentrations were measured with Bradford assay using extinction coefficients of 4.8 $cm^{-1}\mu M^{-1}$ and 3.2 $cm^{-1}\mu M^{-1}$ for Ffh and FtsY, respectively.

Supported Lipid Bilayer. Supported Lipid Bilayer (SLB) was prepared following established protocol with minor modifications (Lin et al. 2010). In brief, 1,2-dioleoyl-sn-glycero-3-phosphocholine (DOPC) and 1,2-dioleoyl-sn-glycero-3-phospho-L-serine (DOPS) chloroform stocks (Avanti Polar Lipids) were mixed in a molar ratio of 95%:5%. The lipid mixture was doped with trace amount of Texas Red 1,2-dihexadecanoyl-sn-glycero-3-phosphoethanolamine (TR-DHPE, Invitrogen) to help focus at the SLB surface. The lipid mixture was dried at 40 °C under vacuum using a rotary evaporator and stored in Argon at –30 °C until use. The dried lipid film was rehydrated in ddH_2O to 0.5 mg/mL and sonicated at ~30% amplitude in an ice-water bath for >3 min with breaks using a microtip to generate small unilamellar vesicles (SUV).

Glass coverslips and microscopic slides were cleaned by 5 minutes of incubation in 3:1 vol/vol mixture of sulfuric acid/30% hydrogen peroxide, thorough rinses with ddH_2O, and dried under vacuum or nitrogen gas. Reaction flow chambers were assembled using the cleaned coverslips and slides. About 20 µL 0.45 mg/mL SUV suspension in TBS buffer (20 mM Tris-HCl, pH 7.5, 136 mM NaCl) was injected into the chamber and incubated at room temperature for 30-60 min. SLB was

formed through self-assembly of SUVs on hydrated glass surfaces. Excess SUVs were washed out with 400 μL TBS buffer. The SLB were imaged on the same day of preparation.

Single-molecule Instrumentation. All single-molecule assays were carried out with an objective-type total internal reflection fluorescence microscope (Olympus X81). Green (532 nm) and red (637 nm) lasers were introduced in a 100X oil immersed objective and focused on the coverslip. Scattering light was removed by a 560 nm and a 660 nm long pass filter (Chroma) for the green and red lasers, respectively. The green laser was used to focus at SLB, which was doped with TR-DHPE. The red laser was used for imaging the protein samples. Movies were recorded using an Ixon 897 camera (Andor).

Single-molecule Imaging Condition. All protein samples, except for the RNCs, were ultracentrifuged at 100,000 rpm (Optima TLX, Beckman Coulter) for 1 hr to remove aggregates. Imaging was carried out in SRP buffer supplemented with oxygen scavenging system (0.4% glucose and 1% Gloxy in Trolox (Roy et al. 2008)). Experiments with free FtsY-Alexa647 used imaging buffer containing 100 μM GppNHp. SRP•FtsY closed complex was assembled with 1 μM labeled FtsY-Alexa647, 3 μM Ffh, 6 μM 4.5 RNA, 100 μM GppNHp in SRP buffer and diluted to 100 pM in imaging buffer containing 100 μM GppNHp. SRP•FtsY early complex was assembled with 200 nM Ffh-Alexa647, 300 nM FtsY, 400 nM 4.S RNA, and 500 nM RNC_{FtsQ} in SRP buffer without Nikkol and diluted to 100 pM in

imaging buffer. The samples were then flowed onto the chamber coated with SLB for imaging. Movies were taken at a frame speed of ~20 ms/frame for 1000 frames (about 20 seconds) in each measurement, to minimize sample heat up and photobleaching. In each experiment, the data were averaged over movies from 10 different observation areas.

Real-time Targeting Assay. Real-time targeting of SRP to the SLB was carried out using similar single-molecule imaging conditions as in the above section with the following modifications. The SLB composition for tethering FtsY-dN1 is 98% DOPC/2% Ni-NTA-DGS (1,2-dioleoyl-sn-glycero-3-[(N-(5-amino-1-carboxypentyl)iminodiacetic acid)succinyl] (nickel salt), Avanti Polar Lipids) doped with trace TR-DHPE. The Ni-SLB was first incubated with 1 μM FtsY-dN1 for 2 min in TBS buffer. Unattached FtsY-dN1 was washed out using 200 μL TBS buffer. The resulting surface density of tethered FtsY-dN1 was 3000-5000/μm^2, which corresponds to a concentration in the imaging chamber of ~200 nM, for comparison with the reaction using 200 nM wildtype FtsY. Targeting reactions were initiated by mixing and injecting 200 nM wildtype FtsY and 200 pM SRP-Alexa647 loaded with RNC into SLB coated chamber, or by injecting 100 pM SRP-Alexa647 loaded with RNC into chambers in which FtsY-dN1 was tethered on the SLB. The RNC concentrations were 100 nM for FtsQ and 500 nM for Luc. The imaging chamber was connected to an automatic pump (NE-1000, New Era Pump System), which was synchronized with the camera for zero time point injection. Time-lapse images were taken at 1 sec intervals with 100 ms exposure

time for about 10 min. Targeting signals were quantified by counting the number of fluorescent spots on SLB from the time-lapse images. The zero drift continuous (ZDC) autofocus system was used to maintain samples in focus during injection and long-time imaging.

Equilibrium Targeting Assay. The targeting selectivity of membrane-tethered FtsY-d14, FtsY-NG+1, and FtsY-NG, along with FtsY-dN1, were tested in a similar setup as in the Real-time targeting assay, where the FtsY variants were pre-assembled to SLB, doped with 2% Ni-DGS, through their N-terminal His_6 tags. The tethering and targeting reaction conditions were the same as described in the previous section. As the targeting reactions finishes in 10 minutes (Figure 2.7B), we only recorded short movies within the 15-20 minute time window of the reaction. The movies were taken at ~50ms/frame speed for 50 frames (~2.5 secs). In each experiment, the data were averaged over movies from > 6 different observation areas.

Data Processing. Trajectories of individual fluorescent spots from single-molecule experiments were extracted using a MATLAB routine combining the 'spotDetector' (Aguet et al. 2013) and the 'Particle Tracking' (Blair & Dufresne 2013) written by Daniel Blair and Eric Dufresne. The extracted trajectories were analyzed using MATLAB. Trajectories from spots with unstable fluorescence intensity and zero mobility were discarded because they likely arise from noise and proteins aggregated at SLB defects, respectively. For real-time targeting assay, the tracking

process was still carried out to identify immobile spots. Trajectories that passed quality control were used for kinetic analysis as described below.

Survival Probability Analysis.

In most single-molecule TIRFM studies, dwell-time histograms are used for extracting kinetic parameters. This approach doesn't apply in our case since individual FtsY molecules were not tethered to the glass coverslip surface, and the short and long trajectories were unevenly sampled within the limited imaging time. Therefore, we defined a parameter, the survival probability ($P_{survival}$), for quantifying the kinetic properties of FtsY-membrane interactions on SLB.

We first define $N(i, j)$ as the number of trajectories observed at the i^{th} frame and lasts another j frames. The survival probability distribution $P_{survival}\,(i, j)$ is then the normalized quantity:

$$P_{survival}(i,j) = \frac{N(i,j)}{N(i,1)}. \qquad (2.1)$$

Since the trajectories sample equilibrium distributions, which are time invariant, this function is independent of i and thus simplifies to $P_{survival}\,(j)$, which can be obtained by time-averaging of the trajectories:

$$P_{survival}(j) = \frac{1}{m-j+1} \sum_{i=1}^{i=m-j+1} P_{survival}\,(i,j). \qquad (2.2)$$

The survival probability distribution as a function of time t, $P_{survival}\,(\mathrm{t})$, was obtained by substituting the frame numbers with t/dt, where dt is the time interval between frames. The $P_{survival}\,(t)$ data were fit to Equation 2.3,

$$P_{survival}(t) = P_1\exp(-k_{-1}t) + P_2\exp(-k_{-2}t), \quad (2.3)$$

in which k_{-1} and k_{-2} are the dissociation rate constants of FtsY molecules from the SLB in the Dynamic and Stable modes, respectively, and P_1 and P_2 are the fraction of molecules exhibiting k_{-1} and k_{-2}, respectively. Photobleaching was estimated from the total fluorescence intensity of fluorescently labeled FtsY, tethered on Ni-DGS SLB through the Ni-His6 interaction. The timescale of photobleaching is much slower than the Stable mode and thus negligible in the analysis (Figure 2.2-Figure supplement 2). However, we note that the derived value of k_{-2} is close to the timescale of the slowest process that could be observed within the 20 second imaging time (to minimize sample heating and dye photobleaching). Thus, the kinetic stability of the Stable mode could be higher than the value of k_{-2} reported here.

Thermodynamic Model of FtsY-Membrane Interactions. To define the thermodynamic cycle of FtsY-membrane interaction, we calculated the equilibrium constants of the two membrane binding modes: $K_x = k_x/k_{-x}$, where x = 1 represents the Dynamic mode and x = 2 represents the Stable mode. The association rate constants (k_x) are related to the apparent association rate constants, $k_{x,app}$ for free FtsY and $k'_{x,app}$ for SRP•FtsY complex, and the fractions of the two modes in solution, f_x and f'_x, respectively, by Equation 2.4.

$$\begin{aligned} k_{x,app} &= f_x \cdot k_x \\ k'_{x,app} &= f'_x \cdot k_x \end{aligned} \quad , x = 1, 2. \quad (2.4)$$

Assuming FtsYs in the Dynamic and the Stable modes are the only two species in solution and their membrane-association rates and equilibrium constants are unaffected by SRP, f_1 and f_2 are constrained by mass conservation $1 = f_1 + f_2$. The same constraint is applied for f'_1 and f'_2. Substituting f_x and f'_x using Equation 2.4 into the mass conservation equations gives Equation 2.5:

$$1 = \frac{k_{1,app}}{K_1 \cdot k_{-1}} + \frac{k_{2,app}}{K_2 \cdot k_{-2}}$$
$$1 = \frac{k'_{1,app}}{K_1 \cdot k_{-1}} + \frac{k'_{2,app}}{K_2 \cdot k_{-2}} \quad (2.5)$$

The values of K_1, K_2, k_1, and k_2 can be obtained by solving Equation 2.5. As the amount of membrane-bound FtsY was <1% of the total number of FtsY even in the SRP·FtsY sample, depletion of FtsY from the solution phase was therefore not considered.

The equilibrium constants between the Stable and Dynamic populations in the cytosol (K_{cyto}) and on the membrane (K_{mem}) for free FtsY are defined as

$$K_{cyto} = \frac{f_2}{f_1}$$

$$K_{mem} = \frac{P_2}{P_1},$$

in which P_1 and P_2 are the membrane-bound populations of FtsY in the Dynamic and Stable modes, respectively, determined from the SLB experiments using a lifetime cutoff of $\tau = 0.25$ sec. The values of f_1 and f_2 were calculated using f_1=

P_1/K_1 and $f_2 = P_2/K_2$, respectively. The same procedure gave the values of K'_{cyto}, K'_{mem}, and f'_x for the SRP·FtsY complex.

GTPase Assay. Assays to measure the stimulated GTP hydrolysis reaction between SRP and FtsY was carried out and analyzed as described (Peluso et al. 2001). Reaction mixtures in SRP buffer were assembled with 100 nM Ffh, 400 nM 4.5S RNA, and 0.1, 0.2, 0.5, 1, 5, 10 μM of FtsY (wildtype or mutants). Lipid-stimulated GTP hydrolysis reactions were measured using 100 nM Ffh, 400 nM 4.5S RNA, 0.2 μM FtsY (full-length or d14), and 0, 0.4, 0.6, 0.8, 1 mg/mL PG/PE liposomes. Reactions were initiated by addition of 100 μM GTP (doped with γ-^{32}P-GTP) and quenched with 0.75 M KH_2PO_4 (pH 3.3) at different time points. The hydrolyzed phosphate and unreacted GTP were separated by thin layer chromatography and quantified by autoradiography. The measured hydrolysis rates were fit to

$$k_{obsd} = \frac{k_{cat}[\mathrm{FtsY}]}{K_m + [\mathrm{FtsY}]}, \qquad (2.6)$$

in which k_{cat} is the rate constant of GTP hydrolysis from the SRP•FtsY complex, and k_{cat}/K_m approximates the association rate constant for SRP-FtsY complex formation.

Co-translational targeting and translocation assay. *A*ssays were carried out as described (Shan et al. 2007; Shen et al. 2012). In brief, 10 μL of *in vitro* translation reactions of pPL in Wheat Germ extract (Promega) containing ^{35}S-methionine were initiated and, within 3 min of initiation, added to a mixture of 200 nM Ffh, 400 nM

4.5S RNA, 0, 14, 36, 71, 214 nM wildtype or mutant FtsY, and 0.5 eq/μL of salt-washed, trypsin-digested microsomal membrane to a total volume of <15 μL. Reactions were quenched by adding 2X SDS-loading buffer and boiling and analyzed by SDS-PAGE followed by autoradiography. The data were fit to

$$\%translocation = \frac{V_{max}[\mathrm{FtsY}]}{K_{1/2} + [\mathrm{FtsY}]}, \qquad (2.7)$$

in which V_{max} is the maximum translocation efficiency at saturating concentrations of FtsY, and $K_{1/2}$ is the concentration of FtsY required to reach half of V_{max}.

Liposome Preparation for Ensemble Assays. A 70 mol% 1-palmitoyl-2-oleoyl-*sn*-glycero-3-phospho-(1'-*rac*-glycerol) (POPG) and 30 mol% 1-palmitoyl-2-oleoyl-*sn*-glycero-3-phosphoethanolamine (POPE) lipid mixture in chloroform was dried as described in SLB preparation. Dried lipid film was rehydrated in buffer containing 10 mM Tris-HCl, pH 8, and 1mM DTT to 10 mg/mL. Large unilamellar vesicles (LUV) were generated using three-rounds of freeze-thaw cycles followed by 21 times extruding through 100 nm pore polycarbonate filters. Aliquots were flash frozen and stored at –80 °C.

Ensemble Fluorescence Measurements. The fluorescence spectra of acrylodan-labeled FtsY were obtained on a Fluorolog-3 spectrofluorometer (Jobin Yvon) with an excitation wavelength of 360 nm. Time-courses of early-to-closed complex rearrangement were measured on a Kintek stop-flow apparatus. The emission signal changes were monitored at 515 nm and 470 nm for samples in the absence and

presence of PG/PE liposomes, respectively. The early complex was pre-assembled with 200 nM FtsY-acrylodon, 15 μM Ffh, 30 μM 4.5S RNA with or without 1 mg/mL PG/PE liposome present. The SRP concentration was varied from 15 to 25 μM to ensure complete formation of the early complex. The closed complex rearrangement was initiated by adding 200 μM GppNHp to early complex mixtures. Time courses of fluorescence changes were fit to single-exponential functions to extract the rearrangement rate constants.

In vivo assays. Wildtype or mutant FtsY with C-terminal His_6-tags were cloned into pTlac18 plasmid using Gibson assembly (Gibson et al. 2009). For details of the construction of pTlac18 vector, see the following sections. The 3L-Pf3 DNA sequence was synthesized by standard polymerase chain reaction using overlapping oligos as described in (Lim et al. 2013), and cloned into FtsY constructs to make TM-fusion FtsYs. The FtsY conditional knockout strain, *E. coli* strain IY28 (Bahari et al. 2007), was a kind gift from the Bibi Lab. IY28 transformed with empty vector or with pTlac18 plasmids encoding wildtype or mutant FtsY were grown to log phase in 2.5 mL LB containing 0.2% arabinose, 100 μg/mL Ampicillin, 50 μg/mL Kanamycin at 37 °C. The cells were harvested by low-speed centrifugation, washed once in LB, and resuspended to OD_{600} = 1 in LB containing antibiotics. Serial dilutions of cell suspensions were plated in 3 μL droplets onto LB plates containing antibiotics and 0.2% arabinose or 1 mM IPTG, or no inducers. The plates were incubated at 37 °C for 14 hr before imaging. Cell fractionation assays were carried out to confirm the expression and localization of the FtsY variants.

pTlac18 Plasmid. The pTlac18 vector is derived from pTrc99A with two modifications: (i) to reduce leaky expression from the *trc* promoter, the -35 elements were mutated from *trp* to *lacUV5* consensus sequences and the spacing between -35 and -10 elements were increased from 17 bp to 18 bp. The resulting promoter sequence is $^{-35}$TT***T***ACAATTAATCAT***T***CCGGCTCGTATAAT^{-10} (-35 and -10 elements are underlined and bold italic fonts indicate the mutation sites); (ii) to make a more stringent selection, an additional Kanamycin resistance site was inserted after the Ampicillin resistance site using Gibson assembly.

Cell Fractionation. Cells were inoculated into 10 mL LB containing antibiotics and 0.5 mM IPTG by diluting 1000-fold from the OD_{600} = 1 suspensions. Cells were grown at 37 °C to OD_{600} ~ 1, washed twice with 10 mL LB, and then pelleted in 1.5 mL eppendorf tubes at amounts equivalent to 1 mL X 3 OD_{600}. The pellets were re-suspended in 900 μL lysis buffer (50 mM HEPES-KOH, pH 8, 100 mM KOAc, 10% glycerol, 1 mM DTT, 1 mM Phenylmethylsulfonyl fluoride, and protease inhibitor cocktail), incubated with 1 mg/mL lysozyme at room temperature for 30 min, and digested with DNAaseI (50 μg/mL in 16 mM $MgCl_2$) on ice for 10 min. Lysed cells were sonicated in a room temperature bath sonicator. Cell debris and unbroken cells were removed by centrifugation at 2k rpm, 5 min in Microfuge 18 (Beckman Coulter). The total lysate sample (T) was taken from the supernatant. The inclusion body (I) was isolated by additional centrifugation at 4k rpm for 5 min. The soluble (S) and membrane (M) fractions were further separated by

ultracentrifugation at 48k rpm for 1 hr in a TLA120.2 rotor (Optima TLX, Beckman Coulter). The inclusion body and membrane samples were dissolved in 5% SDS buffer. All fractions were analyzed using SDS-PAGE and western blotting against the His_6-tag.

Kinetic Simulation. Simulations were carried out in MATLAB by solving the differential equation $\dot{P}(t) = \mathbf{R}P(t)$. P(t) is a vector of populations in each state (*early* and *closed* complex in cytosol or on membrane, plus a downstream targeted state) and **R** is the transition matrix composed of k^*_1, k_{-1}, k^*_2, k_{-2}, k_{switch}^{cyto} and k_{switch}^{mem}. k^*_1 = 1.2 and k^*_2 = 0.115 (μm s^{-1}) are apparent association rate constants derived from k_1 and k_2, respectively, at a membrane surface area of 6 μm^2 and FtsY concentration of 1 μM. All these rate constants were empirically determined from the data in Figures 2.3E and 2.9C. The final targeted state was simulated using a downstream reaction with rate constant of 0.7 s^{-1} (Zhang et al. 2009), in order to drive the directionality of targeting reaction.

FIGURES

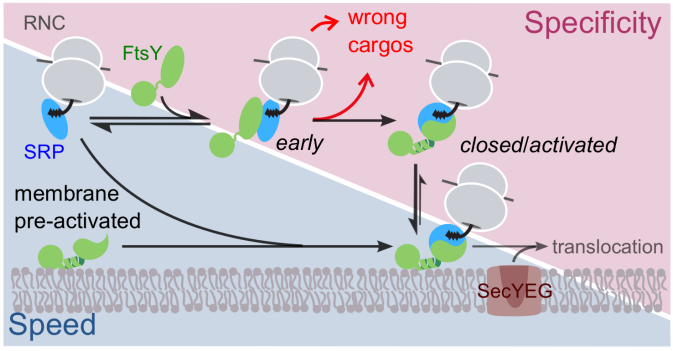

Figure 2.1

Schematic of the current models for co-translational protein targeting by the SRP pathway. Targeting via FtsY molecules that are pre-bound and activated at the membrane is shown on the lower left (shaded in *blue*); the alternative targeting route via FtsY molecules in solution is shown on the upper right (shaded in *magenta*).

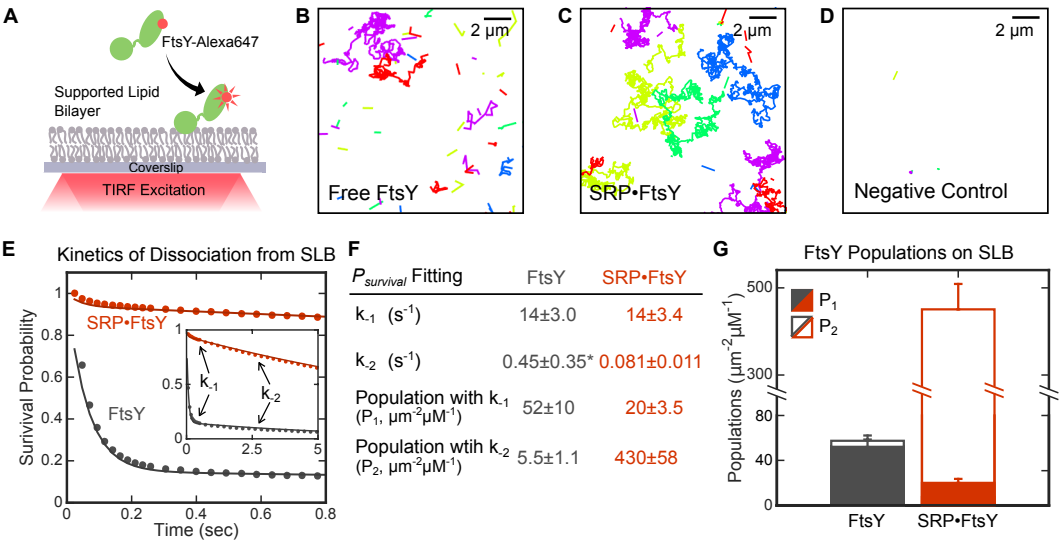

Figure 2.2

Single molecule analyses detected two distinct modes of FtsY-lipid interactions that are regulated by SRP. (**A**) Schematic of smTIRF setup for observing FtsY-membrane interaction on the SLB. FtsY was labeled with Alexa647 at position C345. (**B–D**) Representative trajectories of free FtsY molecules (B), SRP•FtsY complexes (C), and FtsY-dN1 (D) on SLB within an arbitrary section of 100 frames. The colors are randomly assigned to distinguish different molecules. (**E**) Representative data (dots) and fitting curves (lines) of the survival probability distribution of trajectories on SLB for free FtsY (*grey*) and the SRP•FtsY complex (*red*). The data were fit to Equation 2.3, and the obtained parameters were summarized in parts F and G. (**F**) Summary of the dissociation rate constants and population distributions obtained from the survival probability analyses in part E. *The fitting of k_{-2} in free FtsY is only accurate to an order of magnitude, due to the small population of free FtsY in the Stable mode. (**G**) Summary of the population distributions in the Dynamic (filled bars) and Stable (open bars) modes in free FtsY (grey) and the SRP•FtsY complex (red). All values are reported as mean ± S.D., with $n \geq 3$.

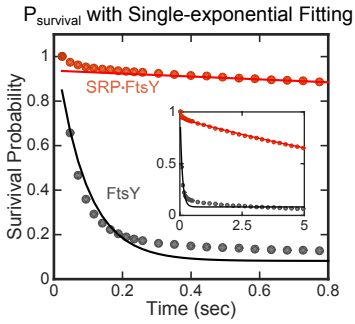

Figure 2.2-Figure supplement 1

Single-exponential functions do not adequately fit $P_{survival}(t)$ data.

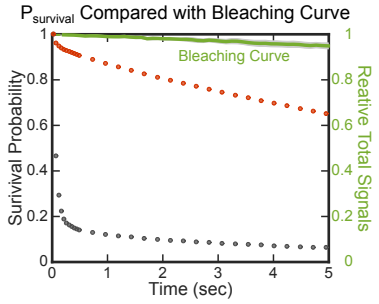

Figure 2.2-Figure supplement 2

Photobleaching is slow and does not interfere with the lifetime analysis. The red and gray dots are the same set of data shown in Figure 2.2E. The green line is the averaged bleaching curve from three movies, determined from the total fluorescence intensity of FtsY tethered on Ni-DGS SLB. Variation in photobleaching is represented by the light gray area around the green line.

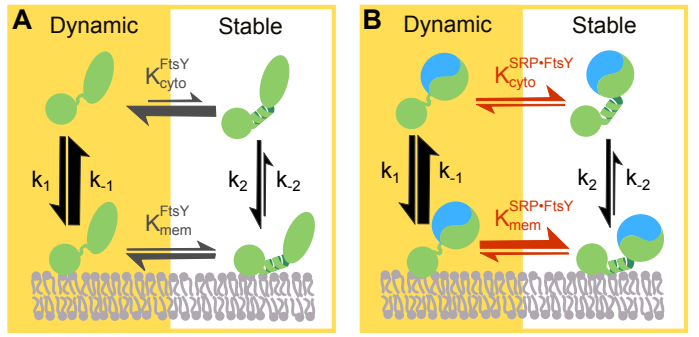

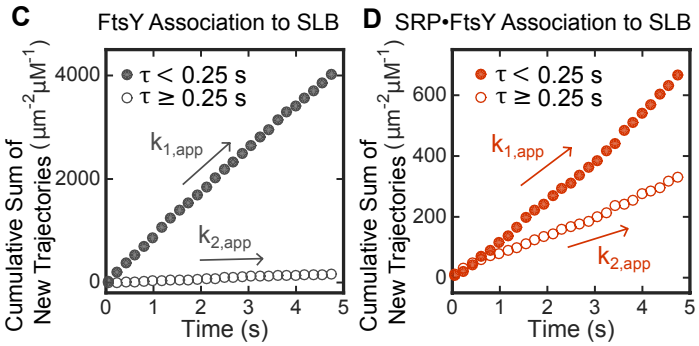

E

	k_{on} ($\mu m^{-2} \mu M^{-1} s^{-1}$)		k_{off} (s^{-1})		K_{cyto}	K_{mem}
	k_1	k_2	k_{-1}	k_{-2}		
FtsY	730	N.D.	14±3.0	0.45±0.35	1.7×10^{-2}	0.22
SRP•FtsY	730	69	14±3.4	0.081±0.011	2.2	30

Figure 2.3

SRP binding drives FtsY from the Dynamic to the Stable mode. (**A, B**) Thermodynamic models of FtsY-membrane interaction in free FtsY (A) and the SRP•FtsY complex (B). (**C, D**) Representative data for apparent association kinetics of FtsY (C) and the SRP•FtsY complex (D) with SLB in the Dynamic (closed circles) and Stable mode (open circles). (**E**) List of the rate and equilibrium constants for the models in parts A and B. N.D., not determined with confidence due to the unstable fitting of k_{-2}. Values are reported as mean ± S.D., with $n \geq 3$.

Analysis using lifetime cutoff 0.25s		FtsY	SRP•FtsY
P_1	($\mu m^{-2} \mu M^{-1}$)	71±12	17±2.4
P_2	($\mu m^{-2} \mu M^{-1}$)	16±5.2	500±75
$k_{1,app}$	($\mu m^{-2} \mu M^{-1} s^{-1}$)	1000±130	230±31
$k_{2,app}$	($\mu m^{-2} \mu M^{-1} s^{-1}$)	16±9.2	52±13

Figure 2.3-Figure supplement

Summary of the population distributions and apparent association rate constants obtained by using a lifetime cutoff of 0.25s to distinguish trajectories in the Dynamic and Stable modes.

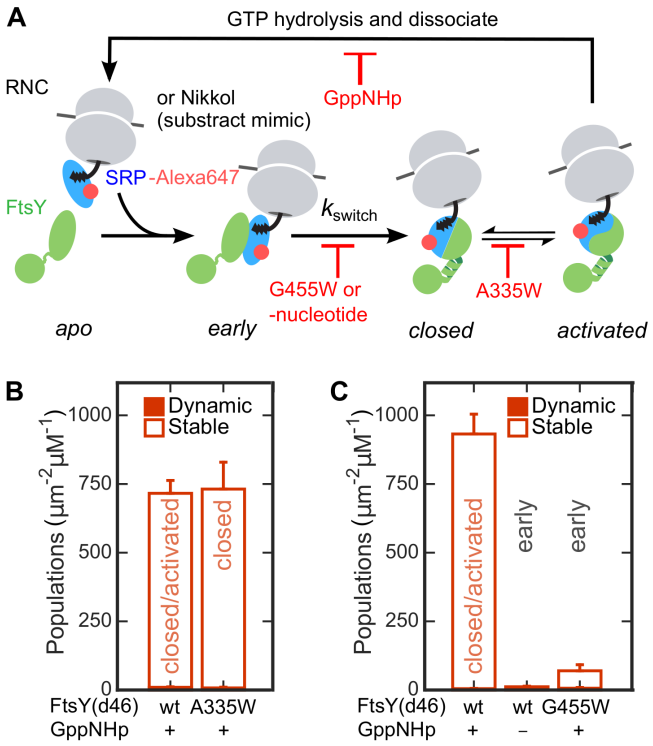

Figure 2.4

The Dynamic-to-Stable transition occurs during the *early*-to-*closed* rearrangement in the SRP•FtsY complex. (**A**) Schematic of conformational changes in the SRP-FtsY GTPase cycle and the conditions that stall the complex at different conformational stages. SRP was labeled with Alexa647 at C153. (**B, C**) Comparison of the lipid interactions of the SRP•FtsY complex with wildtype proteins in GppNHp (a mixture of *closed*/*activated* states) and with the complex stalled in the *closed* state (B) or the *early* state (C). Filled and open bars represent populations in the Dynamic and Stable modes, respectively, determined using the lifetime cutoff of 0.25 seconds. As expression of full-length FtsY(A335W) is toxic to the cell, FtsY-d46 was used for the measurements in these experiments. Except for the lipid interactions, FtsY-d46 behaves identically to full-length FtsY in the SRP/FtsY GTPase cycle and in activation by RNC (Powers & Walter 1997; Zhang et al. 2009). A substrate mimic, Nikkol (Bradshaw et al. 2009), was included in (B) to facilitate complex formation. RNC_{FtsQ} was included in (C) to stabilize the *early* complex. Values are reported as mean ± S.D., with $n \geq 3$.

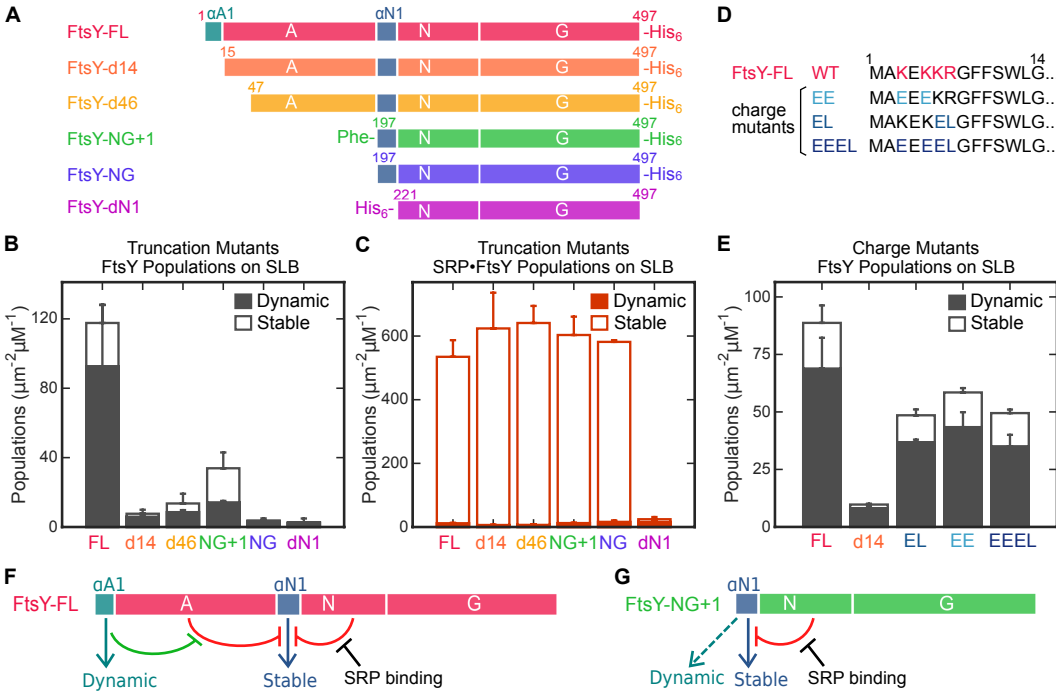

Figure 2.5

Distinct motifs in FtsY mediate the two membrane interaction modes. (**A**) Domain structures of wildtype FtsY and FtsY truncation mutants. (**B, C**) The membrane binding abilities of the truncation mutants on SLB as free FtsY (B) and SRP•FtsY complex (C). Filled and open bars represent populations in the Dynamic and Stable modes, respectively, determined using the lifetime cutoff of 0.25 seconds. (**D**) Sequences of the αA1 motif in wildtype and charge mutants. Charged residues in wildtype sequence are highlighted in *red*, and their mutations are highlighted in *blue*. (**E**) Charge mutations in αA1 reduced membrane interactions of free FtsY with SLB. (**F, G**) Model for regulation of the membrane interactions of full length FtsY (**F**) and FtsY-NG+1 (**G**). Cyan and blue arrows denote membrane interactions in the Dynamic and Stable modes, respectively. Both the A-domain (this work) and N-domain (Parlitz et al. 2007; Lam et al. 2010) inhibit FtsY from engaging the membrane in the Stable mode (red inhibition marks). In full-length FtsY, αA1 partially relieves the inhibition from the A-domain (green inhibition mark). In FtsY-NG+1, the αN1 motif can also mediate some degree of Dynamic interactions

(dashed arrow in **G**). With both constructs, interaction with SRP is the most effective mechanism to relieve the inhibitory effect from the N-domain and allow FtsY to interact with the membrane in the Stable mode. Values are reported as mean ± S.D., with n ≥ 3.

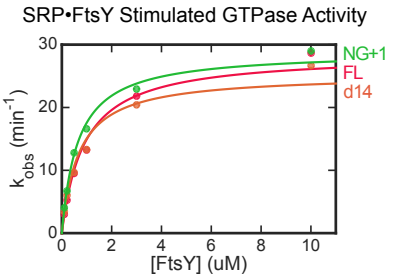

Figure 2.5-Figure supplement 1

FtsY truncation mutants exhibit no defects in complex formation and GTPase activation with SRP in the absence of lipids. Stimulated GTPase reactions of SRP with FtsY were determined as described in Materials and Methods. The data were fit to Equation 6 and gave k_{cat} values of 28.5, 25.3, 28.9 min^{-1} and K_m values of 0.9, 0.7, 0.6 μM for wildtype (FL), d14, and NG+1 mutants of FtsY, respectively.

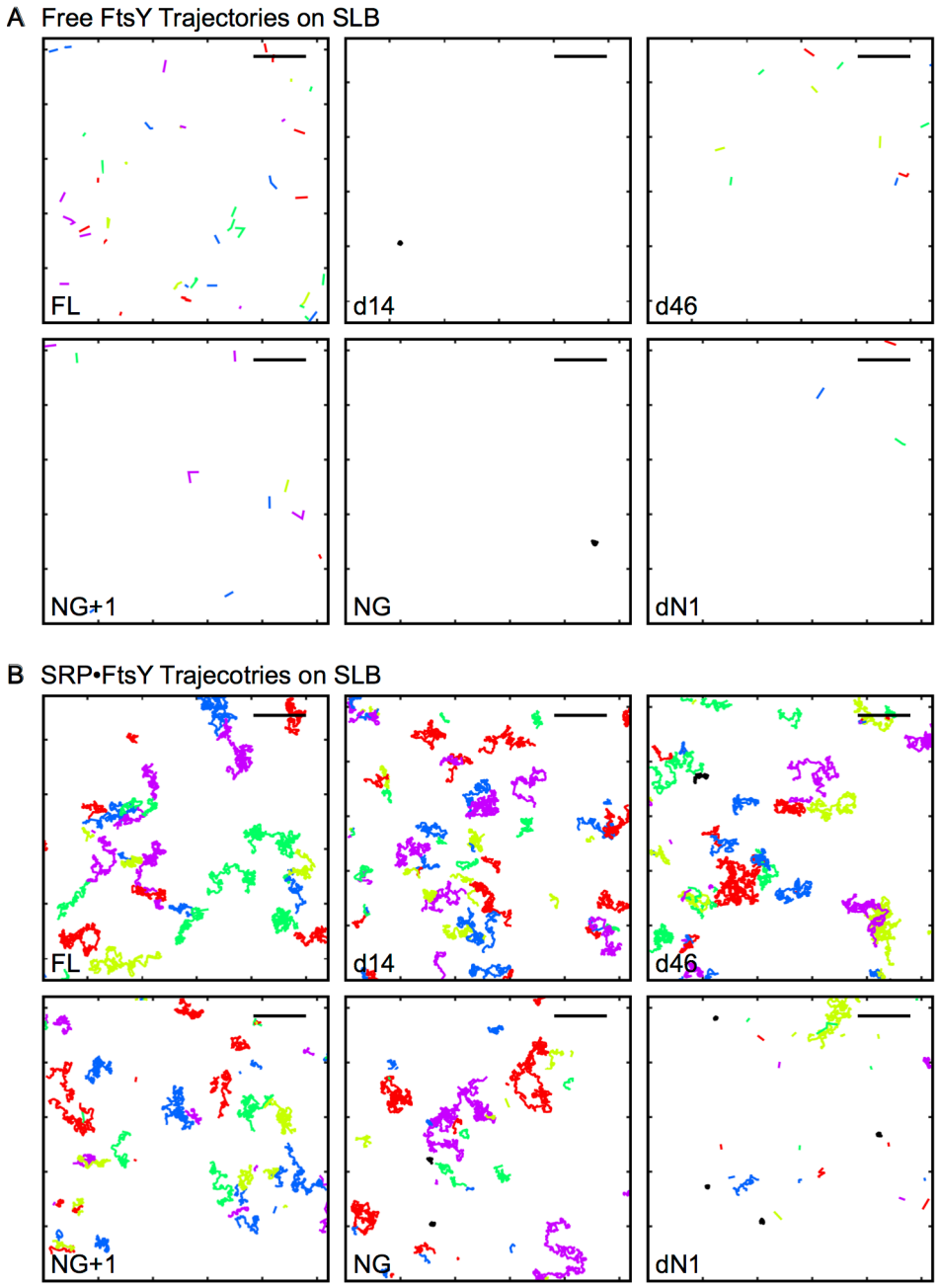

Figure 2.5-Figure supplement 2

Representative trajectories of free FtsY molecules (A) and SRP•FtsY complexes (B) on SLB for wildtype and truncation mutants of FtsY. Trajectories within an arbitrary section of 100 frames are shown. The colors are randomly assigned for distinguishing each trajectory. The scale bars represent 5 μm.

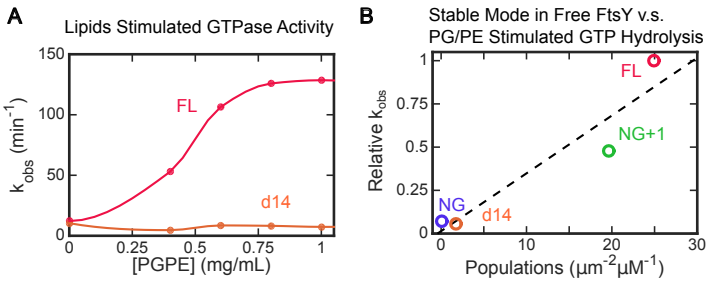

Figure 2.5-Figure supplement 3

Lipid activation of FtsY's GTPase activity independently probes the ability of free FtsY to sample the Stable mode. (A) Lipid activated GTP hydrolysis reactions of full length FtsY and mutant FtsY-d14. (B) Populations in the Stable mode in free FtsY correlate with lipid-stimulated GTPase activity of SRP•FtsY complex. The GTPase rate constants were from part A and from Figure 2.1B in (Lam et al. 2010). All the observed rates (k_{obsd}) at saturating liposome concentrations (>1 mg/mL) were normalized to the values for full-length FtsY measured in parallel.

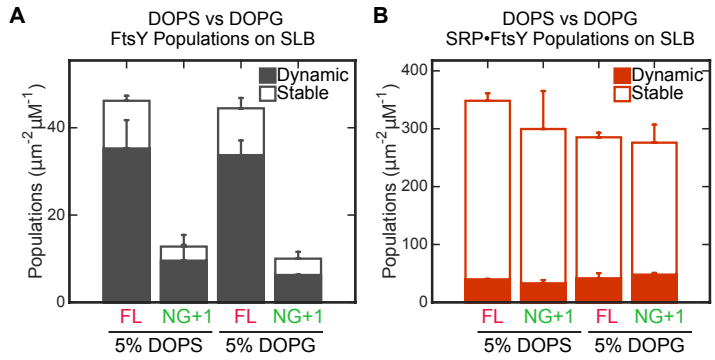

Figure 2.5-Figure supplement 4

The interaction of FtsY with SLB is insensitive to the identity of anionic phospholipids. The binding of full-length (FL) FtsY and FtsY(NG+1) with SLBs generated using DOPC with either 5% DOPS or 5% DOPG were measured for free FtsY (A) and SRP•FtsY complex (B). Filled and open bars represent populations in the Dynamic and Stable modes, respectively.

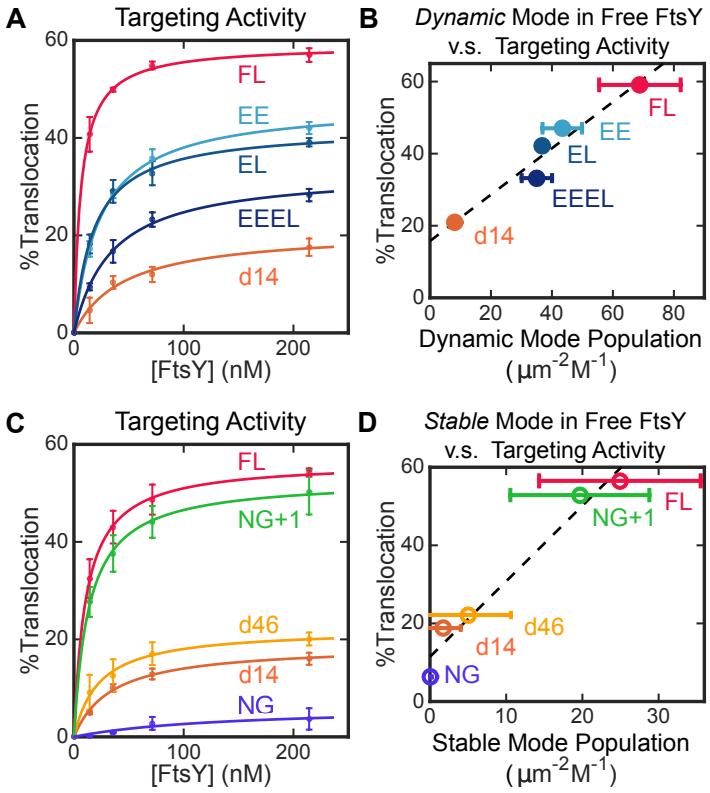

Figure 2.6

Both modes of FtsY-membrane interactions impact efficient protein targeting. (**A**) The effect of charge mutations in the αA1 motif on the co-translational targeting of pPL. Data were fitted to Equation 7. (**B**) Targeting efficiencies of the αA1 charge mutants correlate with the populations of molecules in the Dynamic mode in free FtsY. (**C**) The effect of A-domain truncations on the co-translational targeting of pPL. (**D**) Targeting efficiencies of A-domain truncation mutants parallel their abilities to sample the Stable mode prior to SRP binding. Values are reported as mean ± S.D., with $n \geq 3$.

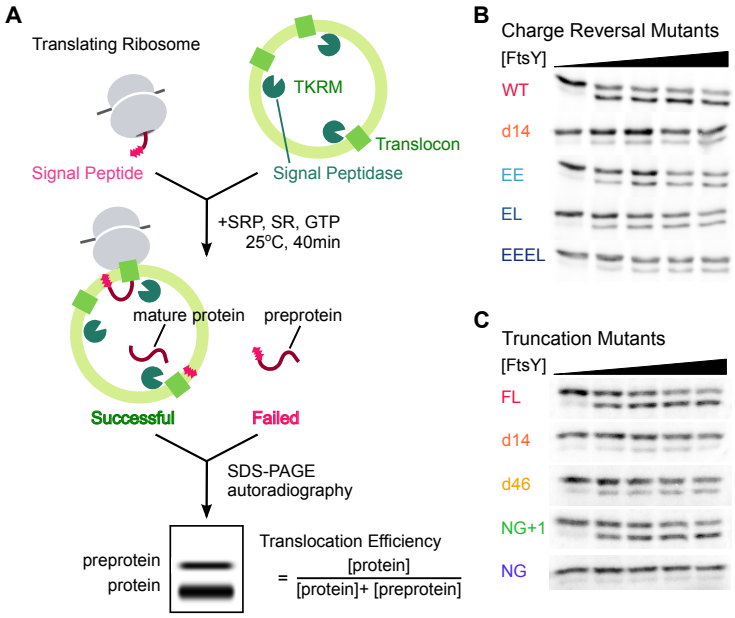

Figure 2.6-Figure supplement

Co-translational protein targeting and translocation by FtsY mutants. (**A**) Schematics of the co-translational targeting and translocation assay using trypsin-treated, high salt-washed endoplasmic reticulum membrane (TKRM). (**B**, **C**) Representative translocation data for FtsY charge-reversal (B) and truncation (C) mutants.

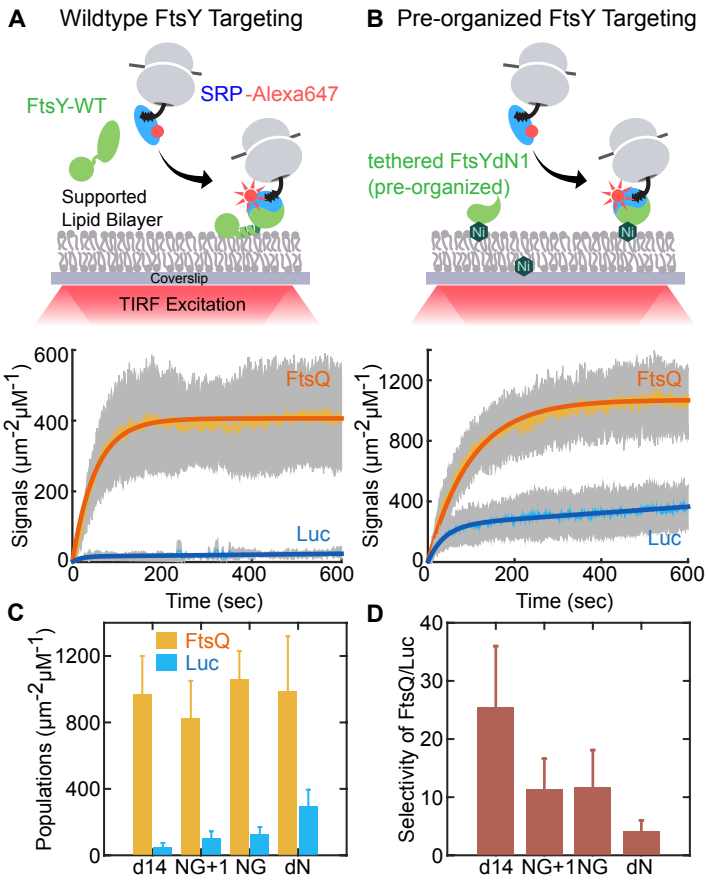

Figure 2.7

An engineered FtsY pre-organized into the Stable mode led to indiscriminate targeting. (**A, B**) Time courses for targeting of RNC_{FtsQ} (*orange*) and RNC_{Luc} (*blue*) to SLB mediated by wildtype FtsY (A) and FtsY pre-organized into the Stable mode (B). Schematics of the single-molecule real-time targeting assay is depicted above. The amounts of FtsY in the two experiments were equalized by adjusting the surface density of tethered FtsY-dN1. (**C**) The amount of RNC_{FtsQ} (orange bars) and RNC_{Luc} (blue bars) targeted to SLB by tethered mutant FtsYs. (**D**) Targeting specificities of SLB-tethered FtsY mutants, defined by the ratio of targeted RNC_{FtsQ} over RNC_{Luc} in (C). Values are reported as mean ± S.D., with $n \geq 3$.

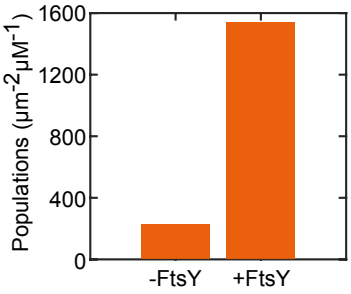

Figure 2.7-Figure supplement

The targeting of RNC_{FtsQ}•SRP to SLB is dependent on FtsY. The amount of RNC_{FtsQ}•SRP targeted to SLB without or with membrane tethered FtsY-dN1 (+FtsY) were tested and quantified**.**

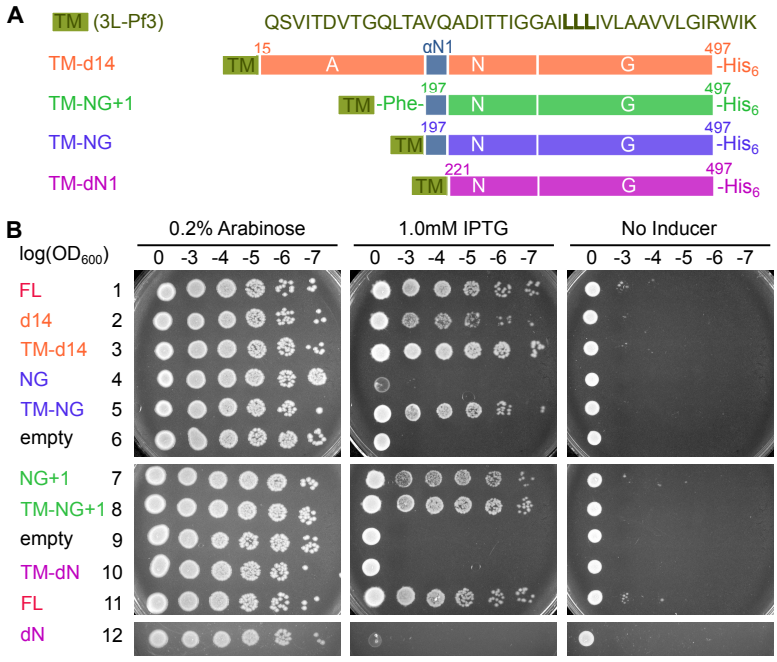

Figure 2.8

Pre-organization into the Stable mode disrupts FtsY function *in vivo*. (**A**) The sequence of the 3L-Pf3 TMD anchor and domain structures of membrane-tethered FtsY mutants (TM-FtsY) used in the *in vivo* assay. (**B**) Frogging assays were carried out to test the ability of mutant FtsYs to complement the loss of genomic FtsY, as described in Methods. Replicates of the data are shown in the Figure supplement.

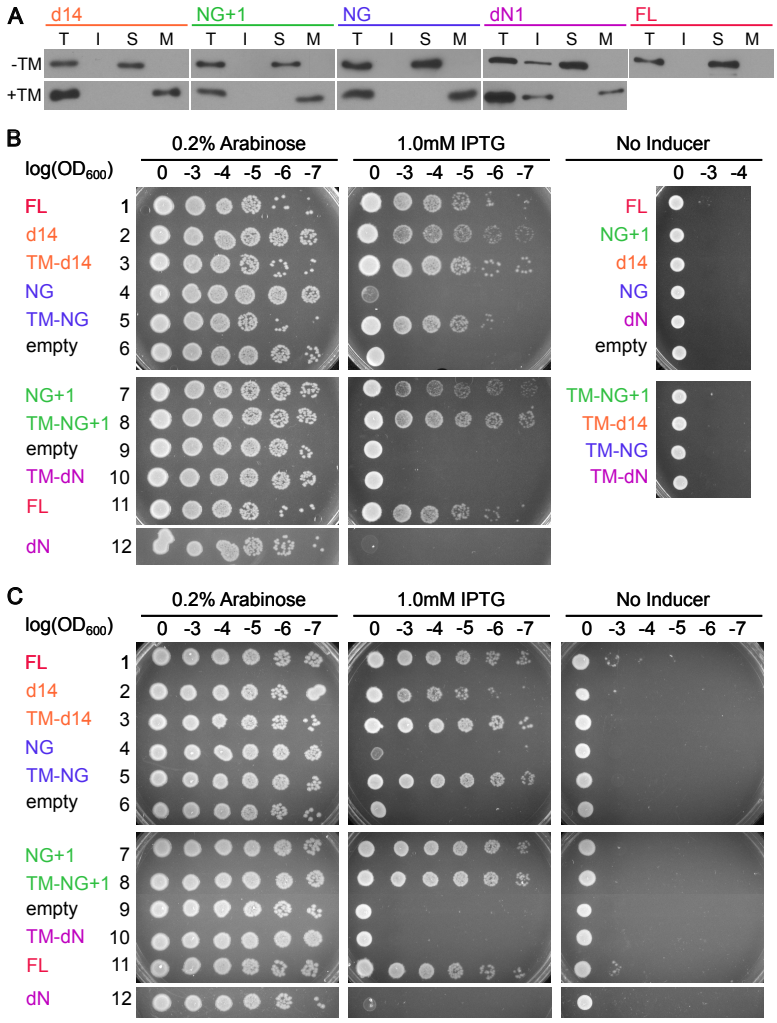

Figure 2.8-Figure supplement

Cell fractionation analyses and replicates of the cell growth assay. (**A**) Cell fractionation analysis to test the effectiveness of membrane tethering by the 3L-Pf3 motif. FtsY truncation mutants without (-TM) or with (+TM) the 3L-Pf3 fusion were expressed and fractionated as described in Methods. Proteins in total (T), inclusion body (I), soluble (S), and membrane (M) fractions were detected via Western-blotting against their C-terminal His_6-tags. (**B, C**) Two independent replicates of the frogging assays (Figure 2.8B) to test the ability of mutant FtsYs to complement FtsY depletion.

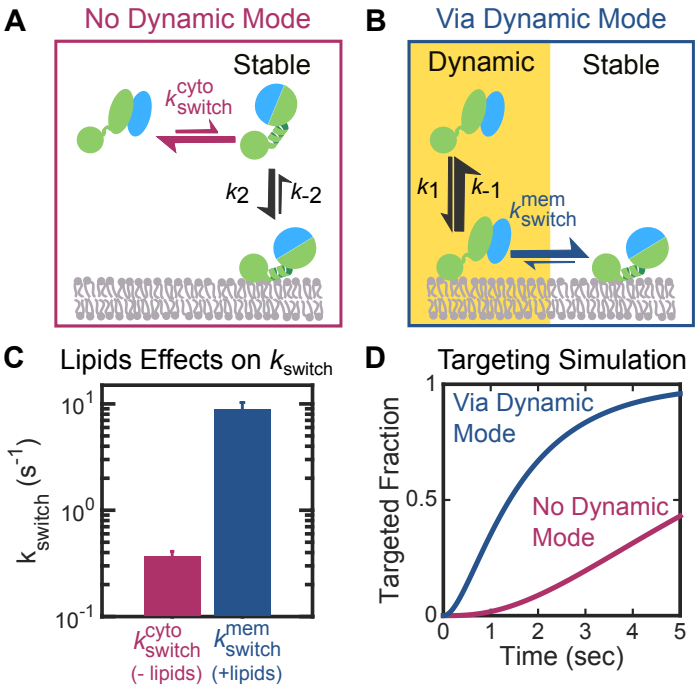

Figure 2.9

The Dynamic mode enables a faster targeting route for FtsY molecules not pre-activated at the membrane. (**A, B)** Depiction of the two thermodynamically equivalent routes to attain the targeting complex bound at membrane in the Stable mode. (**C**) Rate constants for the *early*-to-*closed* rearrangement in the cytosol (k_{switch}^{cyto}) and on the membrane (k_{switch}^{mem}). Values were reported as mean ± S.D. with n = 3. (**D**) Simulation of the kinetics of RNC targeting to membrane via the routes depicted in parts A (*magenta*) and B (*blue*).

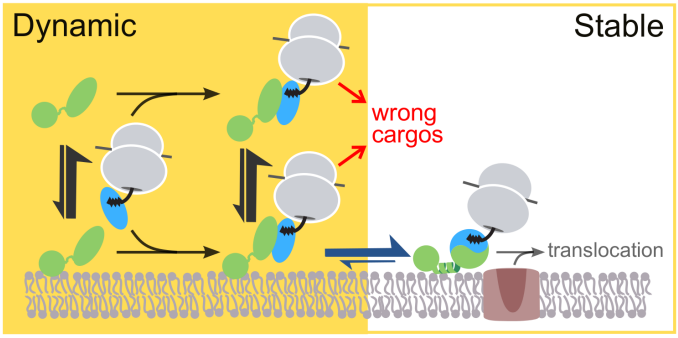

Figure 2.10

Model for the sequential membrane interaction of FtsY during protein targeting, which balances speed and specificity of the pathway. The dynamic mode mediates initial membrane association of free FtsY and the *early* SRP•FtsY complex, followed by rearrangement of the *early* complex to the *closed* state/Stable mode at the membrane. The red arrows depict rejection of SRP-independent substrates before FtsY rearranges to the *closed* state/Stable mode.

Chapter 3: A Molecular Recognition Feature mediates ribosome-induced SRP and SRP receptor assembly during co-translational protein targeting

A version of this chapter was prepared as manuscript of: Hwang Fu Y.H., Chandrasekar S. and Shan S.-O. "A Molecular Recognition Feature mediates ribosome-induced SRP and SRP receptor assembly during co-translational protein targeting." *Submitted.*

ABSTRACT

Molecular Recognition Features (MoRFs) provide interaction motifs in intrinsically disordered protein regions (IDRs) to mediate diverse cellular functions. Here we report that a MoRF element, located in the disordered Linker domain of the mammalian signal recognition particle (SRP) receptor and conserved among eukaryotes, plays an essential role in sensing the ribosome and mediating efficient co-translational protein targeting to the endoplasmic reticulum. Loss of the SRP receptor (SR) MoRF largely abolishes the ability of ribosome to activate efficient SRP-SR assembly and severely impairs co-translational protein targeting. These results demonstrate a novel role for MoRF elements and provide a mechanism for how the ribosome activates the mammalian SRP pathway. Additional comparative analysis with the bacterial SRP further suggests that the SR MoRF replaced the function of the essential GNRA tetraloop in the bacterial SRP RNA, providing an example for the 'export' of RNA function to proteins during the evolution of ancient ribonucleoprotein particles.

INTRODUCTION

The evolution of organisms from bacteria to higher eukaryotes is accompanied by an expansion of intrinsically disordered protein regions (IDRs) in the proteome (Ward et al. 2004; Oldfield et al. 2005). The enrichment of IDRs in the eukaryotic proteome has been attributed to increased needs of transcriptional regulation and cellular signaling in higher eukaryotes. For example, proteins involved in cellular regulation and related to cancer are highly enriched in disordered residue content. In contrast to the canonical structure-function paradigm, IDRs have been shown to mediate critical cellular processes without assuming a preformed stable structure (Oldfield & Dunker 2014; Wright & Dyson 2015; Latysheva et al. 2015). IDRs are characterized by low sequence complexity, low conservation, and biased amino acid compositions lacking bulky hydrophobic residues that promote disorder (Oldfield et al. 2005; Oldfield & Dunker 2014). These features often lead to weak affinities and transient interactions between IDRs and their binding partners, allowing IDRs to mediate dynamic cellular processes such as signaling, complex assembly, or lipid-droplet formation (van der Lee et al. 2014).

IDRs frequently exert their functions via Molecular Recognition Features (MoRFs), which provide interaction sites with binding partners (Mohan et al. 2006; Mészáros et al. 2009; Disfani et al. 2012; Fang et al. 2013; Cumberworth et al. 2013; Fung et al. 2018). MoRFs are short (10-70 residues) segments in IDRs, often presented as “structural dips”, that undergo disorder-to-order transitions upon

binding. MoRFs have been reported as assemblers that recruit interaction partners to an IDR-mediated molecular hub. A prominent example is the p53 interaction network, in which multiple MoRFs in p53 recruit various effector proteins to activate or deactivate downstream signaling pathways (Oldfield et al. 2008). However, the disordered nature of IDRs also present major challenges to the elucidation of their structure, dynamics and activity, and more work is needed to understand the mechanistic principle by which MoRFs mediate diverse cellular functions. Here, we describe a new MoRF element in the intrinsically disordered linker of the Signal Recognition Particle (SRP) receptor, which plays a critical role in sensing and transmitting signals from the ribosome to turn on the SRP targeting pathway.

SRP is a universally conserved targeting machine that co-translationally delivers the majority of membrane and secretory proteins, which compose nearly 30% of the proteome, to the eukaryotic endoplasmic reticulum (ER) or the bacterial plasma membrane (Zhang & Shan 2014; Akopian, Shen, et al. 2013). The targeting process initiates when SRP recognizes an N-terminal signal sequence or the first transmembrane domain of a nascent polypeptide emerging from the ribosome exit tunnel. The interaction of SRP with the SRP receptor (SR) recruits the ribosome-nascent chain complex (RNC) to the target membrane, where the RNC is unloaded onto the Sec61p (or SecYEG in bacteria) translocation machinery, and the nascent protein is integrated into or translocated across the membrane. The most conserved components of SRP and SR can be found in bacteria, where SRP is composed of a

4.5S RNA tightly bound to the SRP54 protein (named Ffh in bacteria). SRP54 contains a methionine-rich M-domain that binds signal sequences on the nascent polypeptide and a special GTPase, NG-domain that dimerizes with a homologous NG-domain in SR (named FtsY in bacteria). Extensive works showed that the GTP-dependent interaction of SRP with FtsY is extensively regulated by the signal sequence and SRP RNA in the bacterial SRP pathway to enable efficient and selective cotranslational protein targeting (Zhang & Shan 2014; Shan 2016). Specifically, RNCs bearing a functional signal sequence pre-organizes SRP into a conformation in which the conserved GNRA tetraloop of the SRP RNA is positioned to contact a basic surface on the NG-domain of FtsY; this contributes a key interaction that enables rapid recruitment of FtsY in response to recognition of the correct cargo (Zhang et al. 2008; Shen & Shan 2010; Shen et al. 2011).

SRP undergoes an extensive expansion in size and complexity during evolution. The mammalian SRP contains a larger 7SL RNA on which five additional protein subunits (SRP19, SRP68/72, and SRP9/14) are assembled. Recent work showed that the interaction between mammalian SRP and SR is accelerated ~100-fold by the 80S ribosome and 20-fold by the signal sequence (Bacher et al. 1996; Lee et al. 2018). The ribosome-induced stimulation is specific to the mammalian SRP and not observed with bacterial SRP, and its underlying molecular mechanism remains incompletely understood. Single-molecule measurements showed that the ribosome unlocks SRP from an auto-inhibited state and allows SRP to sample an active conformation that is conducive to SR binding

(Lee et al. 2018). On the other hand, multiple studies have also implicated the eukaryotic SR in interaction with and potentially sensing the ribosome (Fulga et al. 2001; Legate & Andrews 2003; Bacher et al. 1999; Mandon et al. 2003; Jadhav et al. 2015). While bacterial SR is a single protein in which the SRP-binding NG-domain is preceded by two amphiphilic lipid-binding helices, eukaryotic SR is a heterodimer of SRα and SRβ subunits. SRβ is a single-pass transmembrane protein anchored at the ER. SRα binds tightly to SRβ with its N-terminal X-domain, which is connected to the NG-domain though a ~200-residue intrinsically disordered Linker (Figure 3.1A, wildtype). It was reported that the eukaryotic SR co-sediments with empty 80S ribosomes, and that the SR Linker is important in mediating ribosome binding (Mandon et al. 2003). More recently, Jadhav et al. examined two charged segments in the SR Linker, CBR (residues 129-176) and RBR (residues 205-250) (Figure 3.2A), and suggested that RBR is responsible for ribosome binding (Jadhav et al. 2015). Intriguingly, this study also suggested that CBR helps displace Sec61p from Sec62 in response to the ribosome, perhaps guiding the Sec61p machinery away from SRP-independent pathways.

In this study, we used the recently reconstituted recombinant human SRP and SR to examine the mechanism by which the mammalian SR senses and responds to the 80S ribosome during co-translational protein targeting. We show that a conserved MoRF element in the disordered SR Linker specifically accelerates SRP-SR assembly in response to the ribosome. The role of this MoRF element phenocopies that of the GNRA tetraloop in the bacterial 4.5S RNA, which

accelerates Ffh-FtsY assembly in response to the RNC, whereas the corresponding tetraloop in the mammalian 7SL RNA has lost this stimulatory role. We propose that interactions of the MoRF element in mammalian SR replaces the electrostatic tether provided by the bacterial SRP RNA to stabilize the transition state during SRP-SR interaction. This and other observations suggest that many functions of the bacterial SRP RNA have 'migrated' to protein subunits during the evolution of this ancient ribonucleoprotein particle.

RESULTS

The SR Linker is required for efficient SRP-SR assembly.

To test whether the NG-domain of hSR is sufficient for interaction with SRP, we generated mutant SRs in which individual domains or sequence elements are deleted (Figure 3.1A). SRa-NG contains only the most conserved NG-domain known to dimerize with the homologous NG-domain in SRP54. In SRdX, the X-domain of SRa is deleted, which also abolishes the SRa-SRb interaction. In SRdL, the SR Linker sequence is replaced by a $(GS)_6$ linker. We first used an enzymatic assay to test the effect of these mutations on SRP-SR assembly. The GTPase activity of SRP and SR is stimulated 10^2-10^3 fold when they form a complex with one another, providing a convenient readout of their interactions. Pre-steady-state measurements showed that the observed rate constant of the stimulated GTPase reaction at sub-saturating SR concentrations, k_{cat}/K_m, is rate-limited by and therefore reports on the rate of SRP-SR complex formation (Lee et al. 2018). The rate constant at saturating SR concentrations, k_{cat}, reports on the rate of GTP hydrolysis from a stably formed SRP•SR complex. Reactions were carried out using SRP(4A10L), in which the M-domain of SRP54 is C-terminally fused to a 4A10L signal sequence and in the presence of saturating 80S ribosome. This generates a ribosome- and signal sequence-bound SRP that fully mimics the effect of the RNC in stimulating SRP-SR assembly (Lee et al. 2018).

We recently reported that mutant SRdX is fully functional in mediating rapid recruitment of SR to ribosome and signal sequence-loaded SRP ((Lee et al. 2018)

and Figure 3.1). In contrast, deletion of the SR Linker severely disrupted the SRP-SR interaction, reducing the value of k_{cat}/K_m >20-fold (Figure 3.1B, C). The effects of deleting the SR Linker were similar regardless of whether the SRXb domain was present (Figure 3.1, cf. SRNG versus SRdL), indicating that the linker sequence functions independently of the Xb domain complex (Figure 3.1B, C). In contrast, the value of k_{cat} was affected <2-fold by these mutations (Figure 3.1B, D). These results show that the SR Linker plays a crucial and specific role in efficient complex formation between SRP and SR.

Prediction of a MoRF element in the hSR Linker.

The SR Linker contains ~200 residues and is intrinsically disordered. Based on charge distribution and evolutionary conservation, a previous work suggested the presence of two functional segments in the hSR Linker, CBR (residue 129-176) and RBR (residue 205-250), proposed to regulate the Sec61b-Sec62 interaction and to bind the ribosome, respectively (Jadhav et al. 2015). To identify potential functional motifs in the SR Linker, we analyzed the linker sequence using multiple MoRF predictors including ANCHOR, MoRFpred, and MFSPSSMPred (Mészáros et al. 2009; Disfani et al. 2012; Fang et al. 2013). The three algorithms are based on very different approaches. ANCHOR uses a scoring function that estimates the likelihood of sequences to undergo folding upon binding of globular partners. MoRFpred uses a machine-learning algorithm to make predictions based on a set of sequence properties including evolutionary conservation, predicted disorder, and

selected physicochemical properties of amino acids such as hydrophobicity and charge. MFSPSSMPred uses an algorithm similar to MoRFpred, but weighs sequence conservation more heavily. All three predictors converged on a potential MoRF at residues 242-261 (Figure 3.2A). Sequence alignments of SRa from diverse species also showed that MoRF is the most conserved sequence in the SR Linker (Figure 3.2B and Figure 3.2-Figure supplement 1), consistent with its high scoring in the MFSPSSMPred prediction.

To test the functions of these segments in SR Linker, we generated additional deletion mutants SRdC, SRdR, and SRdM in which the CBR, RBR and MoRF are replaced with $(GS)_6$, respectively (Figure 3.1A). We first tested these mutants in a co-translational protein targeting assay, which examines the ability of recombinant, purified SRP and SR to mediate the targeting and insertion of the model SRP substrate preprolactin into ER microsomes. The microsomes were trypsinized and salt-washed (TKRM) to deplete endogenous SRP and SR (See **Methods** and Figure 3.2-Figure supplement 2). Mutant SRdL was included as a negative control. Despite having the smallest deletion in the SR Linker, SRdM had a much stronger defect in the targeting assay than mutants SRdC and SRdR (Figure 3.2C and Figure 3.2-Figure supplement 2), indicating that the MoRF element contains residues essential for SR function. To further dissect the potential interactions of the MoRF, we mutated conserved residues in this element (R246, W248, L259, and Y261) to alanines. Both mutants SR(RW/AA) and SR(LY/AA) exhibited modest defects in preprolactin targeting, and the combination of all four point mutations,

SR(RWLY/4A), reproduced the targeting defect of SRdM (Figure 3.2D and Figure 3.2-Figure supplement 2). This result strongly suggests that the conserved aromatic and charged residues in the SR MoRF element mediates key molecular interactions during SRP-dependent protein targeting.

SR MoRF and the ribosome synergistically stimulate SRP-SR complex formation.

To understand the role of the SR MoRF element in the targeting reaction, we tested the effects of CBR, RBR, and MoRF deletions on SRP-SR complex formation using the reciprocally stimulated GTPase reaction between SRP and SR (Figure 3.3). In the presence of ribosome- and signal sequence-bound SRP, deletion of MoRF led to a similar defect as deletion of RBR or the entire SR Linker, reducing the k_{cat}/K_m values ~60-fold and the value of k_{cat} by ~3-fold. In contrast, deletion of CBR lead to a modest defect, with a ~4-fold reduction in k_{cat}/K_m and no effects on k_{cat} (Figure 3.3A, filled circles and 3B, filled bars). The similar defects of SRdL, SRdR, and SRdM in k_{cat}/K_m values strongly suggest that the MoRF element is primarily responsible for the role of SR Linker in stimulating efficient SRP-SR assembly.

To test whether MoRF is involved in ribosome-induced stimulation of SRP-SR complex assembly, we measured the stimulated GTPase reactions of signal sequence-bound SRP with wildtype and mutant SRs in the absence of the 80S ribosome (Figure 3.3A and 3B, open circles and bars). Notably, while the ribosome

strongly stimulated complex formation between SRP and wildtype SR (~25-fold, Figure 3.3A-C) as reported previously (Lee et al. 2018), the stimulatory effect of the ribosome was much smaller, ~3-fold, in reactions with mutants SRdL, SRdR, and SRdM (Figure 3.3A-C). The loss of ribosome-induced stimulation of SRP-SR assembly is similar between these three mutants, indicating that the MoRF element is primarily responsible for communication between the SR Linker and the ribosome. In contrast, the stimulatory effect of the ribosome was reduced only ~2-fold in the reaction with SRdC (Figure 3.3). These results show that the MoRF in the SR Linker is a key element that mediates the ribosome-induced activation of SRP-SR complex formation.

MoRF provides a transient interaction to stabilize the transition state of SRP-SR assembly.

To test whether the ribosome and MoRF also affect the equilibrium and kinetic stability of the SRP•SR complex, we used an established Förster Resonance Energy Transfer (FRET) assay based on a donor dye (Cy3B) labeled at SRP54-K47C and an acceptor dye (Atto647N) labeled at the C-terminus of SR. To improve the solubility of labeled SR for fluorescence measurements, we used the SRdX construct in which the SRαX-domain and SRβ are removed (Figure 3.4-Figure supplement 1A). As previously reported, SRdX displayed SRP-SR assembly, GTPase activation, and preprotein targeting activities that are comparable to or slightly higher than SRαβΔTM, and therefore provides a fully functional mimic of

SR for studying the initial assembly between SRP and SR (Lee et al. 2018). We also confirmed that the Linker deletion mutants (SRdC, SRdR, and SRdM) in the SRdX background had the same effects as full-length SRαβΔTM on the stimulated GTPase reaction (Figure 3.4-Figure supplement 1B). This validated the use of SRdX constructs to study the effects of Linker deletions in the fluorescence experiments below.

We first measured the dissociation rate constant (k_{off}) of the SRP•SR complex using pulse-chase experiments. Surprisingly, in the presence of the ribosome, deletion of the MoRF enhanced rather than reduced the kinetic stability of the SRP•SR complex, slowing complex dissociation by ~20-fold (Figs. 4A and 4C, closed circles/bars). The same stabilization was observed with mutant SRdR, whereas the complex assembled with mutant SRdC dissociated at rates similar to that of the wildtype SRP•SR complex (Figs. 4B and 4C, closed circles/bars). In the absence of the ribosome, however, neither the MoRF nor the RBR deletion affected the kinetic stability of the SRP•SR complex (Figs. 4A and B, open circles and Figure 3.4C, open bars). The effects of the SRdM and SRdR mutations on SRP•SR complex dissociation rates as well as the sensitivity of their mutational effects on the 80S ribosome resembles those observed during SRP-SR complex assembly (cf Figure 3.4C and Figure 3.3B). Thus, the MoRF element accelerates both the assembly and disassembly of the SRP•SR complex, and its roles in both processes are dependent on the ribosome.

Additional equilibrium titrations using this FRET assay (Figure 3.4-Figure supplement 2) further revealed that all three SR linker mutants – SRdC, SRdR, and SRdM – weakened the SRP•SR complex, with equilibrium dissociation constants (K_d) 10-20 fold larger than that of wildtype SR (Figure 3.4D; Table 3.2). Unlike the association and dissociation rate constants, the mutational effect on K_d values is larger with SRdC and SRdR, which contain larger deletions of the linker sequence, than with SRdM, suggesting that the observed mutational effects reflect a general role of the linker sequence *after* the SRP•SR complex is assembled. In addition, the effect of these mutations on the equilibrium stability of SRP•SR is not strongly dependent of the ribosome (Figure 3.4D; Tables 3.1 and 3.2). These observations suggest that the SR Linker has a general role in stabilizing the SRP•SR complex at equilibrium, but this role is independent of the MoRF element nor the 80S ribosome; in contrast, the MoRF element exerts its role exclusively during the transition state of SRP-SR complex formation, and its action is synergistic with that of the ribosome.

Attempts to measure the SRP-SR association rate constants (k_{on}) using the FRET assay were unsuccessful with the SR Linker mutants, because hSR co-aggregated with the ribosome at concentrations above 1-2 μM. We therefore calculated k_{on} values from the experimentally determined k_{off} and K_d values ($k_{on} = k_{off}/K_d$). For wildtype SR and mutant SRdM, the calculated k_{on} values are in reasonable agreement with the values of k_{cat}/K_m measured from the GTPase assay (Table 3.1 and 3.2), whereas for mutants bearing larger truncations of the linker

sequence (SRdC and SRdR), the calculated k_{on} values are 10-20 fold lower than the values of k_{cat}/K_m. This is likely due to the use of different SR constructs in the two assays (SRabDTM in the GTPase assay and SRdX in FRET-based assay), and suggests that the SR-Xb domain dimer might partially compensate for large truncations in the SR Linker during complex assembly. Nevertheless, the calculated k_{on} values qualitatively corroborated the conclusions from GTPase assays, that is, mutant SRdM reduced SRP-SR association specifically in the presence of the ribosome (Table 3.2), whereas the same mutation have a much smaller effect without the ribosome present (Table 3.1). The effect of SRdR mutation largely mirrors those of SRdM whereas the mutational effect of SRdC is smaller and largely independent of the ribosome (Tables 3.1 and 3.2), emphasizing that the observed defects in complex assembly can be specifically attributed to the MoRF element.

The SR linker, but not MoRF, mediates ribosome binding.

It was previously proposed that the interaction of mammalian SR with the ribosome allows the latter to provide a template for SRP-SR assembly (Mandon et al. 2003; Jadhav et al. 2015). The simplest molecular model to explain the synergistic effects of MoRF and 80S is that MoRF directly recruits 80S. To test this model, we used a co-sedimentation assay to probe the binding of SR to 80S (Figure 3.5 and Figure 3.5-Figure supplement) and tested the effects of SR linker mutations on 80S binding. The fraction of SR bound to 80S was quantified from the amount

of SRα that co-sedimented with the ribosome in the pellet (P) fraction relative to the concentration of SRα in the total reaction mix (T) (Figure 3.5C). Deletion of either the CBR or RBR led to >2-fold reductions in SR-80S binding (Figure 3.5A and C). In contrast, the two folded domains in SR, Xb and NG, displayed no detectable 80S binding (Figure 3.5B and C). Consistent with these results, mutant SRdX lacking the Xb domain complex retained significant ribosome binding. These results suggest that the SR linker sequence is primarily responsible for the interaction of SR with the 80S ribosome, and the charged CBR and RBR in this linker both provide important ribosome binding sites. To our surprise, deletion of the MoRF led to minimal loss in the 80S binding of SR (Figure 3.5A and C). Thus, the MoRF element does not directly recruit the ribosome to SR, and must mediate the ribosome-induced stimulation of SRP-SR complex formation via other mechanisms.

The electrostatic tethering of SRP RNA to SR is lost in the mammalian SRP pathway

Previous work with the bacterial SRP showed that the conserved GNRA tetraloop of the 4.5S RNA forms a transient electrostatic interaction with a basic surface on the FtsY NG-domain, providing a transient tether that holds the SRP and FtsY together to stabilize the transition state of their assembly (Zhang et al. 2008; Shen & Shan 2010; Shen et al. 2011). The kinetic signatures of the SR MoRF element are highly reminiscent of those of the 4.5S RNA tetraloop in bacterial SRP:

both elements accelerate the association and dissociation of the SRP•SR complex, without significantly impacting the equilibrium stability of the complex (Shen et al. 2011). Moreover, both the SR MoRF and 4.5S RNA tetraloop exert their stimulatory effects in response to the RNC. The GNRA tetraloop is conserved in the mammalian 7SL RNA. We therefore asked if the electrostatic tethering interaction between this RNA tetraloop and SR is preserved or lost in the mammalian SRP pathway.

To address this question, we assembled SRPs carrying mutations in the GNRA tetraloop and tested their effects on SRP-SR assembly using the stimulated GTPase assay between SRP and SR. In bacterial SRP, mutating the RNA tetraloop from GGAA to UUCG reduces the value of k_{cat}/K_m ~200-fold (Zhang et al. 2008). Even more modest mutations, such as GUAA and GUCG, led to ~20-fold and ~50-fold reductions in k_{cat}/K_m, respectively (Figure 3.6A, *E. coli*). In contrast, the k_{cat}/K_m value of human SRP and SR was minimally affected by any of the three tetraloop mutations (Figure 3.6A, Mammalian and Figure 3.6-Figure supplement A & B), indicating that the mammalian SRP-SR interaction is not sensitive to mutations in the RNA tetraloop.

Comparison of the crystal structures of the bacterial and human SRP•SR NG-domain complex (Figure 3.6-Figure supplement C) further showed that the cluster of basic residues (K399, R402, and K406) that comprise the positively charged surface of FtsY that interacts with the 4.5S RNA tetraloop is reduced to a single K537 in the NG-domain of mammalian SR. Moreover, while mutation of K399 in

FtsY reduced the rate of SRP-FtsY complex formation ~100-fold ((Shen & Shan 2010) and Figure 3.6B, *E. coli*), mutation of the corresponding K537 in mammalian SR had a <5-fold effect on the rate of SRP-SR assembly (Figure 3.6B, Mammalian). Together, the results in this section strongly suggest that the mammalian SRP pathway no longer uses the electrostatic tether between the RNA tetraloop and SR to enable rapid SRP-SR complex formation. Instead, the role of this RNA tetraloop is likely replaced by the MoRF element in the SR linker during the evolution of SRP from bacteria to higher eukaryotic organisms.

DISCUSSION

In this work, we identified and characterized a MoRF element in the disordered Linker domain of mammalian SR that specifically accelerates SRP-SR complex assembly in response to the ribosome during co-translational protein targeting. Deletion or mutations of the MoRF led to severe defects in the recruitment of SR to cargo-loaded SRP and in the co-translational targeting of model SRP substrates to the ER. Intriguingly, the roles of the MoRF element in accelerating SRP-SR assembly phenocopy those of the GNRA tetraloop in the bacterial 4.5S RNA, whereas this RNA tetraloop has lost its essential role in the mammalian SRP pathway. We suggest that, in the mammalian SRP pathway, the MoRF element in the SR linker replaces the tetraloop of 4.5S RNA to sense cargo loading on SRP and in response, turn on rapid SRP-SR assembly to mediate the targeting of RNC to the ER membrane.

The kinetic and equilibrium information obtained in this work allow us to construct a free energy diagram that describe the contributions of the ribosome and SR MoRF element to SRP-SR complex formation in a formal model (Figure 3.6C). In the presence of the ribosome, the MoRF element specifically stabilizes the transition state of SRP-SR assembly ~3.2 kcal/mol. Both the association and dissociation of the SRP•SR complex are significantly accelerated, while the equilibrium of complex formation was only affected by ~1.4 kcal/mol (Figure 3.6C, left). The effects of the MoRF are largely lost in the absence of the ribosome (Figure 3.6C, right). Reciprocally, the ribosome stabilizes the transition state during

complex formation with wildtype SRP ~3.1 kcal/mol, and had a more modest effect, ~0.7 kcal/mol, on the equilibrium of complex formation (WT, black lines); these stimulatory effects of the ribosome are largely abolished upon deletion of the MoRF (dM, red line). Thus, the MoRF element and 80S ribosome act synergistically to stabilize the transition state during SRP-SR complex formation.

Stimulation of SRP-SR complex assembly by the 80S ribosome is a eukaryote-specific phenomenon (Lee et al. 2018; Mandon et al. 2003; Bacher et al. 1996), as is the ability of the eukaryotic SR to directly bind the ribosome (Mandon et al. 2003; Jadhav et al. 2015). It was proposed that the 80S ribosome, by contacting both the SRP and SR, could provide a template on which SRP and SR assemble. However, the results here indicate that ribosome binding of SR is largely uncorrelated with the efficiency of SRP-SR complex assembly or co-translational protein targeting. While SRdC and SRdR showed a similarly low affinity to ribosome, the stimulated GTPase hydrolysis and targeting activity of SRdC are much higher than those of SRdR. On the other hand, deletion of SR MoRF had minimal impact on SR-ribosome binding, but severely disrupts SRP-SR complex assembly and co-translational protein targeting (c.f. Figure 3.5C and Figure 3.2C). These mutational results also ruled out the possibility that the SR MoRF exerts its stimulatory role by helping to recruit the ribosome. Instead, our results suggest that this element specifically senses and transmits the information of ribosome binding to the SRP and SR GTPases to turn on their interactions, probably by optimizing

the positioning of the SR NG-domain with respect to the SRP54-NG near the ribosome exit site to promote their assembly (Figure 3.6E).

The following observations strongly suggest that the MoRF in the mammalian SR Linker replaces the 4.5S RNA tetraloop in the bacterial SRP to stimulate the recruitment of SR to cargo-loaded SRP. In bacteria, the RNA tetraloop interacts with the basic surface on the bacterial FtsY NG-domain to form a transient electrostatic tether that stabilizes the transition state during complex assembly (Figure 3.6D). Mutation of either the charged residues in FtsY or the RNA tetraloop significantly impacts SRP and FtsY interactions (Figure 3.6A and B, *E. coli*). In contrast to bacterial SRP, the assembly of mammalian SRP and SR is not sensitive to either of these mutations, suggesting that the electrostatic tethering mechanism is no longer employed in the mammalian SRP system (Figure 3.6A and B, Mammalian). Together with the similarities in kinetic signatures of the effects of SR MoRF and the 4.5S RNA tetraloop, it's reasonable to propose that the role of the RNA tetraloop in bacterial SRP is replaced by the MoRF element in mammalian SRP. In addition, the functions of multiple other elements in the bacterial SRP RNA are carried out by protein subunits in eukaryotic SRP. For example, the eukaryotic-specific SRP9/14 mediates interaction of the Alu-domain at the elongation factor binding site to regulate translation elongation, whereas the Alu-domain of SRP is comprised solely of RNA in gram positive bacteria (Halic et al. 2006; Beckert et al. 2015; Mary et al. 2010). Additionally, in a recent structure of a 'pre-handover' mammalian RNC-SRP-SR ternary complex, the SRP-SR NG-

domain complex moves to the distal site of 7SL RNA after their initial assembly and form a network of interactions with SRP68/72 and the X- and b-domains of SR (Kobayashi et al. 2018). The analogous distal site movement of the NG-domain complex in bacterial SRP is mediated exclusively by interactions with the SRP RNA (Ataide et al. 2011). Collectively, these observations support a model in which the functions of RNA in this ancient ribonucleoprotein particle are exported to new protein subunits during its evolution in higher eukaryotic organisms. MoRF elements in IDRs could play an important role in this functional 'export', by virtue of their ability to mediate weak, transient, but specific interactions encoded by the amino acid sequence.

MATERIAL AND METHODS

Vector, protein and RNA preparations. Plasmids for recombinant expression of SRP protein and RNA subunits, SRαβΔTM, and SRdX have been described (Lee et al. 2018). Plasmids for expression of mutant SRs and mutant 7SL RNAs were constructed using the QuikChange mutagenesis protocol (Stratagene). Recombinant wildtype and mutant hSRs were expressed from *E. coli* and purified as previously described (Lee et al. 2018). Reconstituted hSRP and hSRP(4A10L) were assembled from individually expressed/purified hSRP proteins and *in vitro* translated/gel purified 7SL RNA as described in the previous study (Lee et al. 2018). 80S ribosomes were purified from Rabbit Reticulocyte Lysate (RRL) as described in (Lee et al. 2018). Preprolactin (pPL) mRNAs for *in vitro* translation-translocation assays were synthesized by *in vitro* transcription using SP6 polymerases following the Megascript protocol (Ambion). Cyslite hSRP54(K47C) was labeled with Cy3B maleimide (Invitrogen) and purified as described (Lee et al. 2018). Wildtype and mutant hSRdX(R458A) constructs were labeled with Atto647N (Invitrogen) through the C-terminal sortase-tag as described in (Lee et al. 2018). For all the biochemical experiments, hSRs were centrifuged at 4 °C, 100,000 rpm in TLA100 rotor for 30 minutes to remove aggregates before the assay.

GTPase assay. GTPase reactions were performed in SRP Assay Buffer (50 mM KHEPES (pH 7.5), 200 mM KOAc, 5 mM $Mg(OAc)_2$, 10% glycerol, 2 mM DTT, and 0.02% Nikkol) at 25 °C. Reactions were followed and analyzed as described

before (Lee et al. 2018). The reciprocally stimulated GTPase reaction between SRP and SR were measured under multiple turnover conditions using 0.15 μM hSRP(4A10L), 0.2 μM 80S when indicated, varying concentrations of hSR, and 100 μM GTP doped with trace γ-^{32}P-GTP. The SR concentration dependences of observed rate constants (k_{obsd}) were fit to Equation 3.1, where k_{cat} is the GTPase rate constant at saturating SR concentration and K_m is the SR concentration required to reach half of the maximal observed GTPase rate constant.

$$k_{obsd} = k_{cat} \times \frac{[SR]}{K_m + [SR]} \quad (3.1)$$

Co-translational targeting and translocation assay. Assays were carried out as described (Lee et al. 2018). In brief, 8.5 μL of *in vitro* translation reactions of preprolactin in Wheat Germ extract (Promega) containing ^{35}S-methionine were initiated and, within 3 minutes of initiation, added to a mixture of 30 nM hSRP, 0, 5, 10, 40, 100 nM wildtype or mutant hSR, and 0.5 eq/μL of salt-washed, trypsin-digested microsomal membrane (TKRM) to a total volume of <15 μL. Reactions were quenched by adding 2X SDS-loading buffer and boiling after 40 minutes of initiation, and analyzed by SDS-PAGE followed by autoradiography. The efficiency of translocation was quantified as Equation 3.2,

$$\%\text{Translocation} = \frac{\text{PL}}{\text{PL} + \frac{7}{8} \times \text{pPL}} \times 100, \quad (3.2)$$

where prolactin (PL) and preprolactin (pPL) amounts are from integrated band intensities on the autoradiography gel image (Figure 3.2-Figure supplement 2).

Fluorescence FRET measurements. All reactions were measured in Assay Buffer (50 mM KHEPES (pH 7.5), 150 mM KOAc, 5 mM $Mg(OAc)_2$, 10% glycerol, 0.03%BSA, 2 mM DTT, and 0.04% Nikkol) at 25 °C. All fluorescence measurements used SRs carrying R458A mutation, which specifically blocks GTP hydrolysis to enable measurements of SRP-SR assembly and disassembly. The values of k_{off} were determined using pulse chase experiments on a stopped-flow apparatus (Kintek) with wildtype SR and a Fluorolog-3 spectrofluorometer (Jobin Yvon) with mutant SRs. The SRP-SR complex were preformed using 12.5 nM labeled hSRP and 1 μM hSR wildtype/mutant SR in the presence of 1mM GTP, and in the presence or absence of 50 nM 80S. Excess unlabeled hSR wildtype was added to initiate complex dissociation. For mutant hSRs, the fluorescence signal change was corrected by subtracting the background signal change in a parallel reaction in which the same volume of buffer was added. The time courses of fluorescence change were fit to the following exponential functions (Equations 3.3 and 3.4) to extract dissociation rate constants (k_{off}). F_{obsd} is the measured donor fluorescence signal, F_{AMP} is the total fluorescence change, F_0 is the initial fluorescence value at time zero, and t is time. Double exponential function (Equation 3.3) was used for fitting measurements of SR wildtype and SRdC in the presence of ribosome. All the other samples were fitted to a single exponential function (Equation 3.4).

$$F_{obsd} = F_{AMP}(1 - \exp(-k_{off1}t) - \exp(-k_{off2}t)) + F_0 \quad (3.3)$$

$$F_{obsd} = F_{AMP}(1 - \exp(-k_{off}t)) + F_0. \quad (3.4)$$

The equilibrium dissociation constants (K_d) of hSRP•hSR complexes were measured on a Fluorolog-3 spectrofluorometer. The equilibrium titrations were carried out using 12.5 nM Cy3B-labeled hSRP, 1mM GTP, and addition of increasing concentrations of Atto647N-labeled hSR wildtype or mutants. Donor fluorescence was recorded when equilibrium is reached. The signal change was corrected by subtracting the background signal of a control titration with unlabeled hSR wildtype/mutants carried out in parallel. The fluorescence signal was converted to FRET efficiency (E) as Equation 3.5,

$$\mathrm{E} = 1 - \frac{\mathrm{F}_{DA}}{\mathrm{F}_{D0}}, \qquad (3.5)$$

where F_{D0} and F_{DA} are the initial value and titrant response of the donor fluorescence signal, respectively. SR concentration dependence of E was plotted and fitted to Equation 6 to extract the dissociation constant (K_d). E_{max} is the value of E at saturating SR concentration.

$$\mathrm{E} = \mathrm{E}_{\max} \times \frac{[\mathrm{SR}]}{K_\mathrm{d} + [\mathrm{SR}]} \qquad (3.6)$$

SR-80S cosedimentation assay. Binding reactions were carried out in 50 mM KHEPES (pH 7.5), 100 mM KOAc, 5 mM $Mg(OAc)_2$ and 1 mM DTT at 25 °C. 400 nM hSR were incubated with 150 nM 80S in a 50 µL reaction volume for 10 min. The mixture was loaded onto a 110 µL 1M sucrose cushion, and ultracentrifuged at 100k rpm for 2 hours in a TLA100 rotor. The pellet fractions were resuspended in 20 µL 1X SDS loading buffer. Equal amounts of the Total and

Pellet samples were loaded on 10% SDS PAGE gels. The gels were coomassie-stained, scanned on a LI-COR odyssey imager at wavelength of 700nm, and intensities of the bands of interest were quantified. For hSR-Xβ and SR-NG, which do not resolve well from ribosomal proteins, the bands were detected and quantified by western-blot against the His_6-tag at the N-terminus of hSRα.

TABLES

Table 3.1

Summary of the rate and equilibrium constants of the SRP-SR interaction for wildtype and mutant SRs in the absence of 80S ribosome.

-80S	WT	dC	dR	dM
K_d (μM)	0.220 ± 0.019	2.547 ± 0.068	2.785 ± 1.147	0.463 ± 0.013
k_{off} (s^{-1})	3.7 (±0.35)×10^{-3}	6.3 (±0.40)×10^{-3}	4.4 (±0.31)×10^{-3}	4.5 (±0.35)×10^{-3}
k_{on} calculated ($M^{-1}s^{-1}$)	1.68×10^4	2.46×10^3	1.61×10^3	9.72×10^3
k_{on} by k_{cat}/K_m ($M^{-1}s^{-1}$)	7.8 (±1.5)×10^4	4.8 (±0.87)×10^4	9.2 (±2.1)×10^3	8.4 (±3.5)×10^3

Table 3.2

Summary of the rate and equilibrium constants of the SRP-SR interaction for wildtype and mutant SRs in the presence of 80S ribosome.

+80S	WT	dC	dR	dM
K_d (μM)	0.071 ± 0.011	1.091 ± 0.031	1.710 ± 0.029	0.809 ± 0.008
k_{off} (s^{-1})	0.220 ± 0.0068	0.123 ± 0.0144	0.014 ± 0.0011	0.010 ± 0.0003
k_{on} calculated ($M^{-1}s^{-1}$)	3.09×10^6	1.13×10^5	7.94×10^3	1.29×10^4
k_{on} by k_{cat}/K_m ($M^{-1}s^{-1}$)	2.0 (±0.27)×10^6	5.7 (±1.3)×10^5	3.6 (±0.34)×10^4	3.5 (±0.89)×10^4

FIGURES

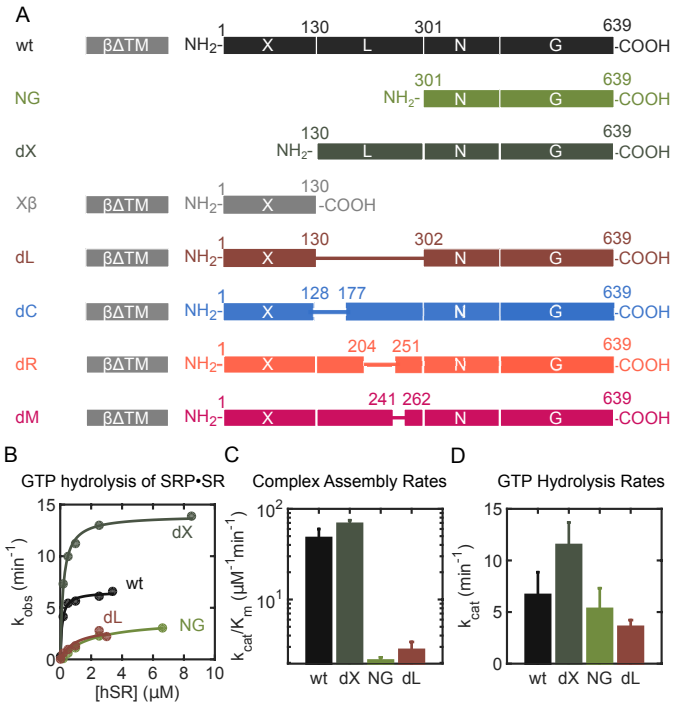

Figure 3.1

(**A**) Domain structures wildtype and mutant SRs used in this study. The transmembrane domain of SRβ was removed to make a soluble SR (Lee et al. 2018). In SRdL, SRdC, SRdR, and SRdM, the deleted sequences are replaced by a $(GS)_6$ linker. (**B-D**) Representative SR concentration dependences of the reciprocally stimulated GTPase reaction between SRP and SR for wildtype SR and indicated SR mutants are shown in (B). The lines are fits of the data to Equation 3.1 in the **Methods**, and the obtained k_{cat}/K_m and k_{cat} values are reported in (C) and (D), respectively. All values are reported as mean ± S.D. with n ≥ 2.

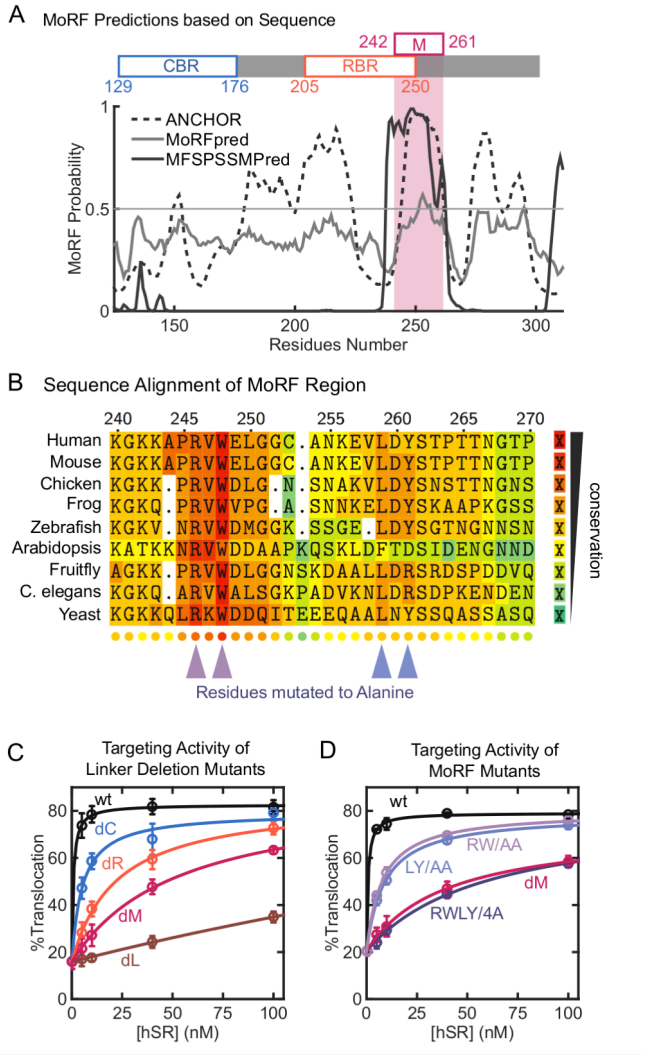

Figure 3.2

(**A**) Probability of MoRF elements in SR Linker generated using sequence analysis software ANCHOR (dashed line), MoRFpred (gray line), and MFSPSSMPred (black line). A schematic representation of SR Linker is shown on top of the MoRF probability plot and aligned to the residue index. CBR, RBR, and the predicted MoRF are highlighted. Note that the MoRF partially overlaps with RBR. (**B**) Sequence alignment of the SR MoRF region were generated with T-coffee webserver (Notredame et al. 2000) and plotted using TeXshade package (Beitz 2000). The arrows below indicate the four conserved residues R246, W248, L259,

Y261 in the MoRF. (**C**, **D**) The effects of SR Linker deletions (C) and MoRF mutations (D) on the co-translational targeting of preprolactin to TKRM. Translocation efficiencies were calculated from Equation 3.2 in the **Methods** and the image data in Figure 3.2-Figure supplement 2. All values are reported as mean ± S.D. with $n \geq 3$.

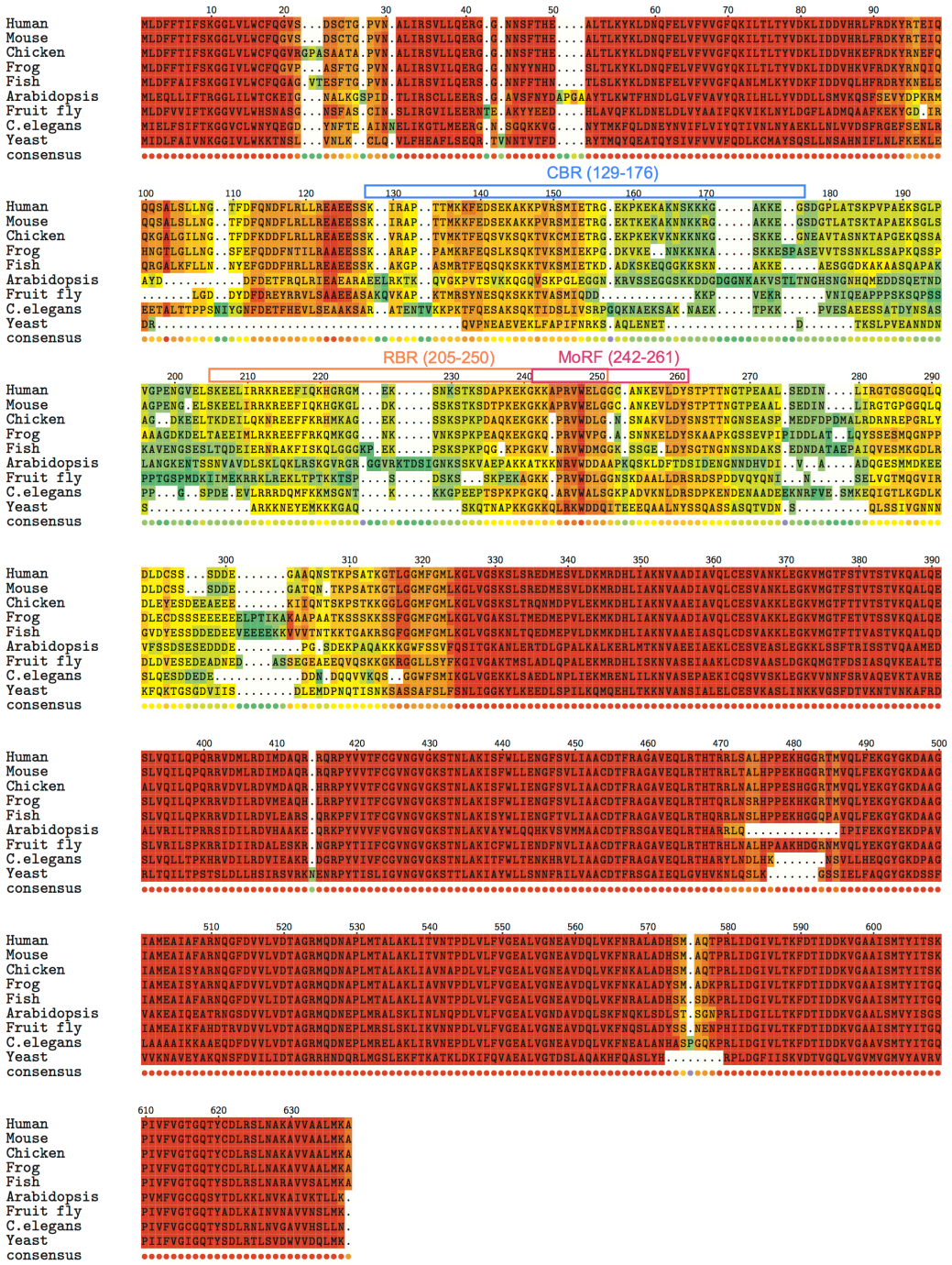

Figure 3.2-Figure supplement 1

Sequence alignment of full-length eukaryotic SRα generated using T-coffee webserver (Notredame et al. 2000) and plotted using TeXshade package (Beitz 2000).

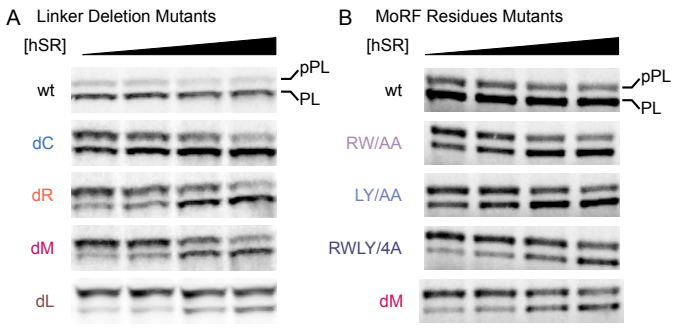

Figure 3.2-Figure supplement 2

Representative SDS-PAGE-autoradiography images for co-translational targeting and translocation of preprolactin into TKRM mediated by hSRP and wildtype SR or the indicated mutants of SR. ‘pPL’ and ‘PL’ denote preprolactin and signal sequence-cleaved prolactin, respectively.

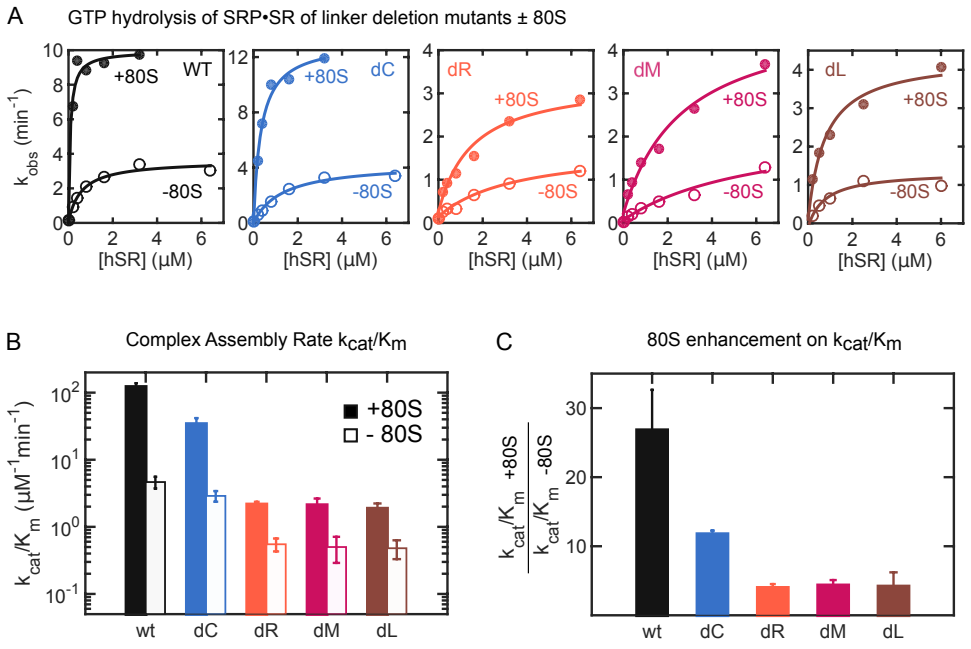

Figure 3.3

(**A**) Representative hSR concentration dependences of the reciprocally stimulated GTPase reaction between SRP and wildtype or mutant SR in the presence (+80S, closed circles) and absence (–80S, open circles) of the ribosome. The lines are fits of the data to Equation 3.1 in the **Methods**. (**B**) Summary of the k_{cat}/K_m values from the stimulated GTPase reactions of SRP with wildtype SR or indicated SR mutants, obtained from the data in (A) and their replicates. Solid and open bars denote reactions in the presence and absence of the ribosome, respectively. (**C**) Summary of the stimulatory effects of the ribosome on the k_{cat}/K_m values, calculated from the data in (B). Values are reported as mean ± S.D. (in part B) or mean ± propagated error (in part C), with $n \geq 2$.

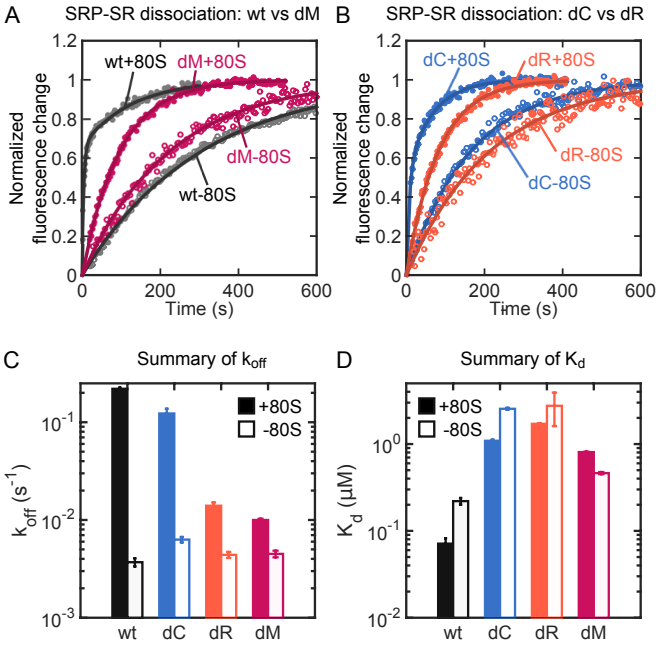

Figure 3.4

(**A**, **B**) Representative time courses for dissociation of the SRP•SR complex for wildtype SR (gray, panel A) and mutants dM (red, panel A), dC (blue, panel B) and dR (orange, panel B) with (closed circles) and without (open circles) the ribosome present. The time courses for wildtype SR and SRdC in the presence of the ribosome were fit to a double exponential equation (Equation 3.3 in **Method**), and dissociation rate constants of the fast phase were reported. All other time courses were fit to a single exponential equation (Equation 3.4 in **Method**). (**C**) Summary of the dissociation rate constants (k_{off}) of the SRP-SR complex formed with wildtype and mutant SRs in the presence (solid bars) and absence (open bars) of the ribosome. (**D**) Summary of the equilibrium dissociation constants (K_d) of the SRP-SR complex formed with wildtype and mutant SRs in the presence (solid bars) and absence (open bars) of the ribosome. The K_d values are derived from the equilibrium titrations shown in Fig. S3. All values are reported as mean ± S.D. with $n \geq 2$.

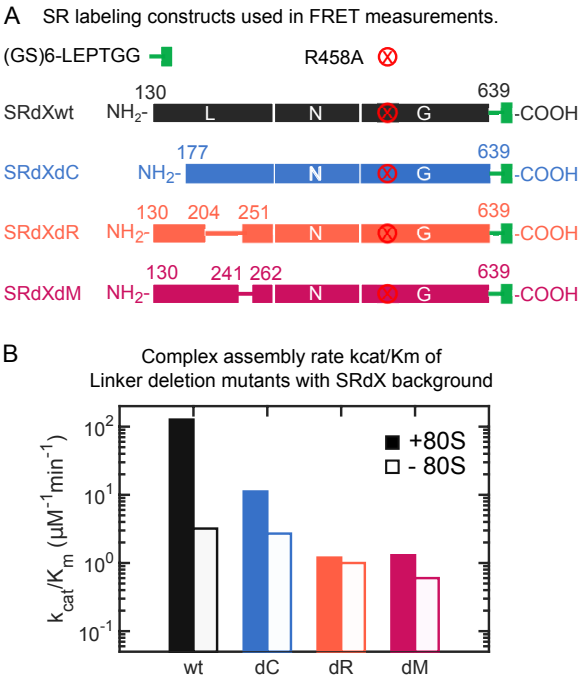

Figure 3.4-Figure supplement 1

(**A**) Domain structures of SR Linker deletion constructs based on the SRdX construct used in FRET measurements. The X-domain is removed for better protein solubility after labeling. Green symbols denote the C-terminal Sortase-tags for fluorescence labeling. Red crosses denote the R458A mutation to block GTP hydrolysis. (**B**) Summary of k_{cat}/K_m values of stimulated GTPase activity of wildtype SRdX and indicated SR Linker deletion mutants based on the SRdX construct. Solid and open bars are reactions in the presence and absence of ribosome, respectively. Consistent with observations with the SRαβΔTM constructs, the k_{cat}/K_m values of SRdR and SRdM were not stimulated by 80S, while SRdC moderately sensed 80S stimulation. The GTPase assays were carried out using the same constructs shown in (A) except for the lack of the R458A mutation.

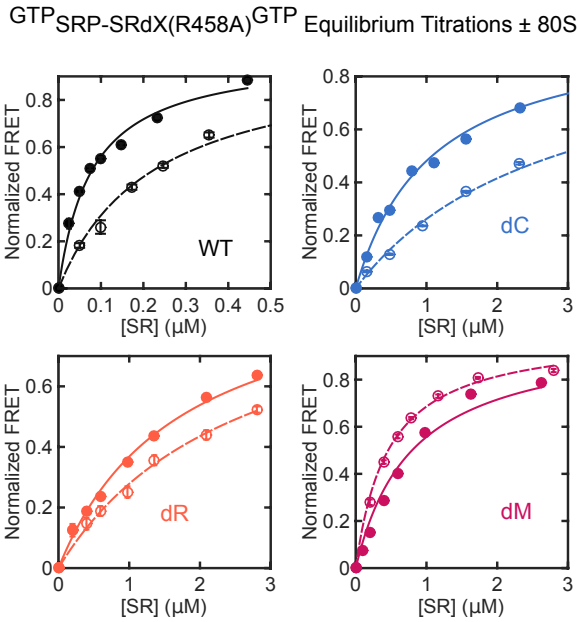

Figure 3.4-Figure supplement 2

Equilibrium titration curves to measure the binding of SRP to wildtype SR (gray) and mutants SRdC (blue), SRdR (orange), and SRdM (red) with (closed symbols) and without (open symbols) ribosome present. All values are reported as mean ±S.D., with $n \geq 3$.

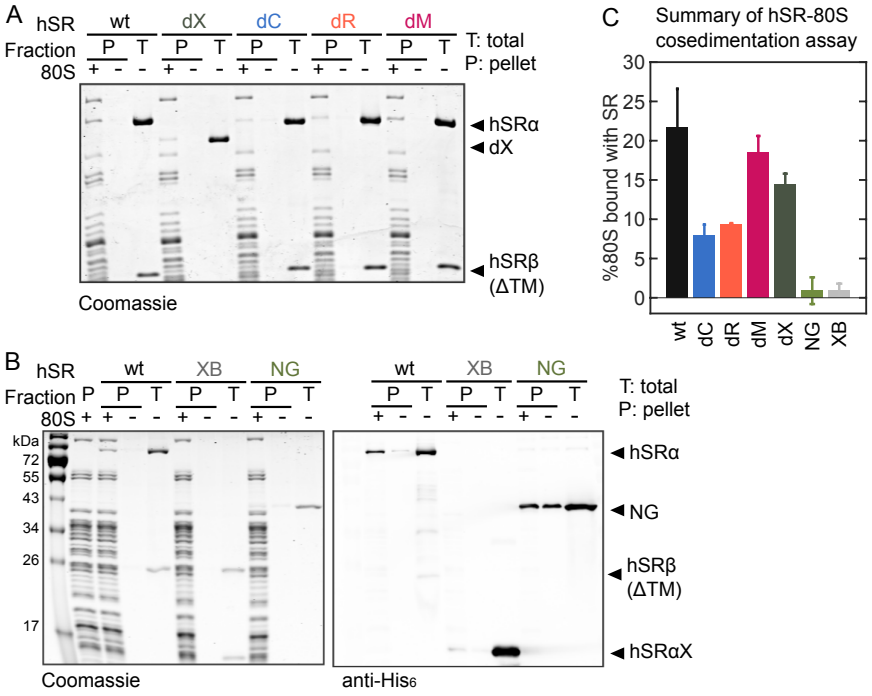

Figure 3.5

(**A**) A representative coomassie-stained gel showing the co-sedimentation of wildtype SR and SR linker deletion mutants with the 80S ribosome. "P" denotes the pellet fraction; "T" denotes the total reaction input of SR. (**B**) Representative coomassie-stained gel (left) and western-blot analyses (right) showing the cosedimentation of full-length SR and the folded domains in SR with the 80S ribosome. (**C**) Quantification of the efficiency of SR cosedimentation with the ribosome. All values are reported as mean ± S.D., with n = 2 for SR-XB and SR-NG, and n ≥ 3 for all other SR constructs. Duplicates and triplicates of the gel images are shown in Figure 3.5-Figure supplement.

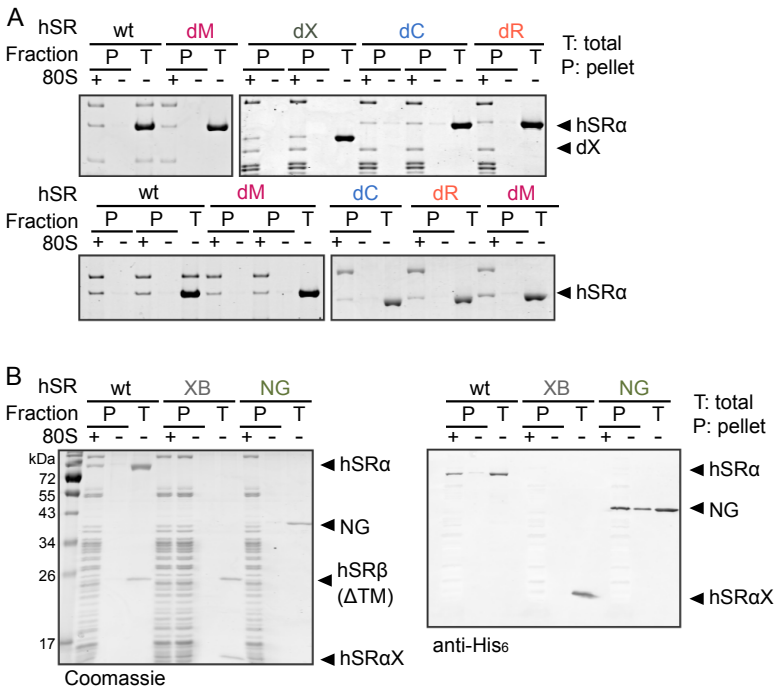

Figure 3.5-Figure supplement

(A) Additional coomassie-stained gels showing the cosedimentation of wildtype SR and SR linker deletion mutants with the 80S ribosome. (B) Additional coomassie-stained gel (left) and western-blot analysis (right) showing the cosedimentation of full-length SR and the folded domains in SR with the 80S ribosome.

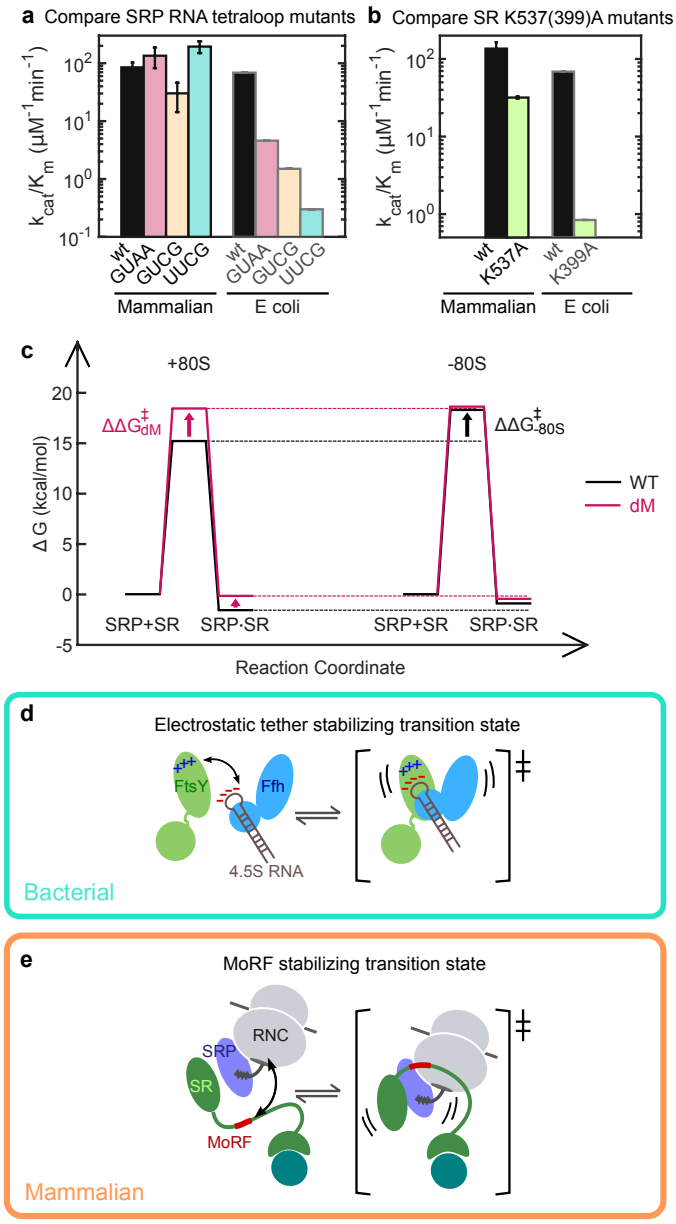

Figure 3.6

(**A**) Summary of k_{cat}/K_m values for the stimulated GTPase reactions of mammalian SRP-SR with wildtype 7SL RNA and the indicated tetraloop mutants. The values are compared to the published k_{cat}/K_m values for reactions of *E. coli* SRP and FtsY with wildtype 4.5S RNA and the same tetraloop mutants (Zhang et al. 2008). (**B**) Summary of k_{cat}/K_m values for the stimulated GTPase reaction of mammalian SRP-

SR with wildtype SR and mutant SR(K537A). The values are compared to published k_{cat}/K_m values for the reactions of *E. coli* SRP-FtsY with wildtype FtsY and the homologous FtsY(K399A) mutant (Shen et al. 2011). All values are reported as mean ± S.D. with n ≥ 3. (**C**) The free energy profile for SRP-SR complex formation in the presence (left, +80S) and absence (right, -80S) of the ribosome for wildtype SR (black lines) and mutant SRdM (red lines). Activation energies were estimated from the measured equilibrium dissociation constants (K_d), measured dissociation rate constants (k_{off}), and calculated association rate constants ($k_{on} = k_{off}/K_d$) using $\Delta G = -RT \ln(k\hbar/k_B T)$, where R = 1.986 (cal $K^{-1}mol^{-1}$), T = 298 (K), $\hbar = 1.58 \times 10^{-37}$ (kcal s^{-1}) and $k_B = 3.3 \times 10^{-27}$ (kcal K^{-1}), using a standard state of 1 μM SR. (**D**, **E**) Comparison of the role of the 4.5S RNA tetraloop and the SR MoRF in stabilizing the transition state of SRP-SR complex assembly in the bacterial (D) and mammalian (E) SRP pathway, respectively.

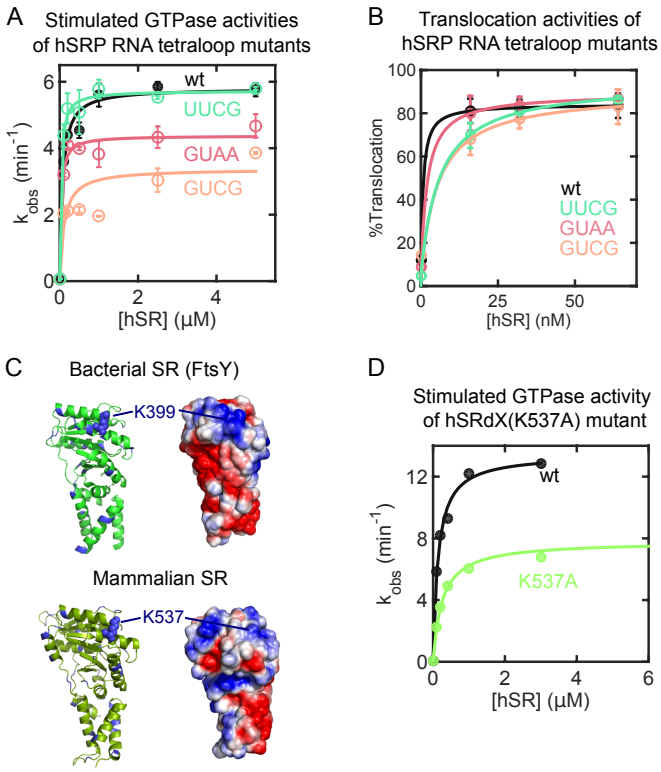

Figure 3.6-Figure supplement

(**A**) Summary of hSR concentration dependences of the reciprocally stimulated GTPase reaction between hSR and hSRP assembled with wildtype 7SL RNA or RNAs carrying indicated tetraloop mutations. (**B**) Mutations in hSRP RNA tetraloop have mild effects on co-translational targeting of preprolactin to TKRM. (**C**) The crystal structures of FtsY (PDB: 4C7O) and human SR (PDB: 5L3Q) are shown in cartoon representation and in electrostatic potential surface (scale ± 2kT/e). Positively charged residues (Lysines and Arginines) are highlighted in blue. The conserved K399 (FtsY) or K537 (hSR) residues are indicated. (**D**) Representative hSR concentration dependence of the reciprocally stimulated GTPase reaction between hSRP and hSR wildtype or hSR(K537A) mutant.

References

Aguet, F. et al., 2013. Advances in analysis of low signal-to-noise images link dynamin and AP2 to the functions of an endocytic checkpoint. *Developmental Cell*, 26(3), pp.279–291.

Akopian, D., Dalal, K., et al., 2013. SecYEG activates GTPases to drive the completion of cotranslational protein targeting. *The Journal of Cell Biology*, 200(4), pp.397–405.

Akopian, D., Shen, K., et al., 2013. Signal Recognition Particle: An Essential Protein-Targeting Machine. *Annual Review of Biochemistry*, 82, pp.693–721.

Angelini, S. et al., 2006. Membrane binding of the bacterial signal recognition particle receptor involves two distinct binding sites. *The Journal of Cell Biology*, 174(5), pp.715–724.

Angelini, S., Deitermann, S. & Koch, H.-G.G., 2005. FtsY, the bacterial signal-recognition particle receptor, interacts functionally and physically with the SecYEG translocon. *EMBO reports*, 6(5), pp.476–481.

Ariosa, A.R. et al., 2013. Fingerloop activates cargo delivery and unloading during cotranslational protein targeting. *Molecular Biology of the Cell*, 24(2), pp.63–73.

Ataide, S.F. et al., 2011. The crystal structure of the signal recognition particle in complex with its receptor. *Science*, 331, pp.881–6.

Bacher, G. et al., 1996. Regulation by the ribosome of the GTPase of the signal-recognition particle during protein targeting. *Nature*, 381, p.248.

Bacher, G., Pool, M. & Dobberstein, B., 1999. The Ribosome Regulates the Gtpase of the β-Subunit of the Signal Recognition Particle Receptor. *The Journal of Cell Biology*, 146(4), p.723.

Bahari, L. et al., 2007. Membrane Targeting of Ribosomes and Their Release Require Distinct and Separable Functions of FtsY. *Journal of Biological Chemistry*, 282, pp.32168–32175.

Beckert, B. et al., 2015. Translational arrest by a prokaryotic signal recognition particle is mediated by RNA interactions. *Nature Structural & Molecular Biology*, 22, pp.767–773.

Beitz, E., 2000. TEXshade: shading and labeling of multiple sequence alignments using LATEX2 epsilon. *Bioinformatics*, 16(2), pp.135–139.

Bibi, E. et al., 2001. Putative integral membrane SRP receptors. *Trends in Biochemical Sciences*, 26(1), pp.15–16.

Blair, D. & Dufresne, E., 2013. Matlab Particle Tracking. Available at: http://site.physics.georgetown.edu/matlab/

Bradshaw, N. et al., 2009. Signal sequences activate the catalytic switch of SRP RNA. *Science*, 323(5910), pp.127–130.

Braig, D. et al., 2011. Signal sequence-independent SRP-SR complex formation at the membrane suggests an alternative targeting pathway within the SRP cycle. *Molecular Biology of the Cell*, 22(13), pp.2309–23.

Braig, D. et al., 2009. Two cooperating helices constitute the lipid-binding domain of the bacterial SRP receptor. *Journal of Bolecular Biology*, 390(3), pp.401–413.

Cremer, P.S. & Boxer, S.G., 1999. Formation and Spreading of Lipid Bilayers on Planar Glass Supports. *The Journal of Physical Chemistry B*, 103(13), pp.2554–2559.

Cross, B.C. et al., 2009. Delivering proteins for export from the cytosol. *Nature Reviews of Molecular Cell Biology*, 10(4), pp.255–264.

Cumberworth, A. et al., 2013. Promiscuity as a functional trait: intrinsically disordered regions as central players of interactomes. *Biochemical Journal*, 454(3), pp.361–369.

Disfani, F.M. et al., 2012. MoRFpred, a computational tool for sequence-based prediction and characterization of short disorder-to-order transitioning binding regions in proteins. *Bioinformatics*, 28(12), pp.75–83.

Draycheva, A. et al., 2016. The bacterial SRP receptor, FtsY, is activated on binding to the translocon. *Molecular Microbiology*, 102(1), pp.152–167.

Egea, P.F. et al., 2004. Substrate twinning activates the signal recognition particle and its receptor. *Nature*, 427, pp.215–221.

Eitan, A. & Bibi, E., 2004. The core Escherichia coli signal recognition particle receptor contains only the N and G domains of FtsY. *Journal of Bacteriology*, 186(8), pp.2492–2494.

Erez, E. et al., 2010. Genetic evidence for functional interaction of the Escherichia coli signal recognition particle receptor with acidic lipids in vivo. *Journal of Biological Chemistry*, 285(52), pp.40508–40514.

Fang, C. et al., 2013. MFSPSSMpred: identifying short disorder-to-order binding regions in disordered proteins based on contextual local evolutionary conservation. *BMC Bioinformatics*, 14, p.300.

Focia, P.J. et al., 2004. Heterodimeric GTPase core of the SRP targeting complex. *Science*, 303(5656), pp.373–377.

Fulga, T.A. et al., 2001. SRbeta coordinates signal sequence release from SRP with ribosome binding to the translocon. *The EMBO Journal*, 20(9), pp.2338–2347.

Fung, H.Y.J., Birol, M. & Rhoades, E., 2018. IDPs in macromolecular complexes: the roles of multivalent interactions in diverse assemblies. *Current Opinion in Structural Biology*, 49, pp.36–43.

Gawronski-Salerno, J. & Freymann, D.M., 2007. Structure of the GMPPNP-stabilized NG domain complex of the SRP GTPases Ffh and FtsY. *Journal of Structural Biology*, 158, pp.122–128.

Gibson, D.G. et al., 2009. Enzymatic assembly of DNA molecules up to several hundred kilobases. *Nature methods*, 6(5), pp.343–345.

Gold, V.A.M. et al., 2010. The action of cardiolipin on the bacterial translocon. *Proceedings of the National Academy of Sciences*, 107(22), pp.8–13.

Halic, M. et al., 2006. Signal recognition particle receptor exposes the ribosomal translocon binding site. *Science*, 312(5774), pp.745–747.

Hopfield, J.J., 1974. Kinetic proofreading: a new mechanism for reducing errors in biosynthetic processes requiring high specificity. *Proceedings of the National Academy of Sciences*, 71(10), pp.4135–4139.

Jadhav, B. et al., 2015. Mammalian SRP receptor switches the Sec61 translocase from Sec62 to SRP-dependent translocation. *Nature Communications*, 6.

Johansson, M., Lovmar, M. & Ehrenberg, M., 2008. Rate and accuracy of bacterial protein synthesis revisited. *Current Opinion in Microbiology*, 11(2), pp.141–147.

Johansson, M., Zhang, J. & Ehrenberg, M., 2012. Genetic code translation displays a linear trade-off between efficiency and accuracy of tRNA selection. *Proceedings of the National Academy of Sciences of the United States of America*, 109(1), pp.131–136.

Kobayashi, K. et al., 2018. Structure of a prehandover mammalian ribosomal SRP·SRP receptor targeting complex. *Science*, 360(6386), pp.323–327.

Kuhn, P. et al., 2015. Ribosome binding induces repositioning of the signal recognition particle receptor on the translocon. *The Journal of Cell Biology*, 211(1), pp.91–104.

Lam, V.Q. et al., 2010. Lipid activation of the signal recognition particle receptor provides spatial coordination of protein targeting. *The Journal of Cell Biology*, 190(4), pp.623–35.

Latysheva, N.S. et al., 2015. How do disordered regions achieve comparable functions to structured domains? *Protein Science*, 24(6), pp.909–922.

Lee, J.H. et al., 2018. Sequential activation of human signal recognition particle by the ribosome and signal sequence drives efficient protein targeting. *Proceedings of the National Academy of Sciences*, 115(24), pp.5487–5496.

van der Lee, R. et al., 2014. Classification of intrinsically disordered regions and proteins.

Chemical Reviews, 114(13), pp.6589–6631.

de Leeuw, E. et al., 2000. Anionic phospholipids are involved in membrane association of FtsY and stimulate its GTPase activity. *The EMBO Journal*, 19(4), pp.531–541.

Legate, K.R. & Andrews, D.W., 2003. The β-Subunit of the Signal Recognition Particle Receptor Is a Novel GTP-binding Protein without Intrinsic GTPase Activity. *Journal of Biological Chemistry*, 278, pp.27712–27720.

Lim, B. et al., 2013. Heat Shock Transcription Factor σ32 Co-opts the Signal Recognition Particle to Regulate Protein Homeostasis in E. coli. *PLoS Biology*, 11(12), p.e1001735.

Lin, W.-C.C. et al., 2010. Supported membrane formation, characterization, functionalization, and patterning for application in biological science and technology. *Current Protocols in Chemical Biology*, 2(4), pp.235–269.

von Loeffelholz, O. et al., 2013. Structural basis of signal sequence surveillance and selection by the SRP-FtsY complex. *Nature Structural & Molecular Biology*, 20, pp.604–610.

Maeda, I. et al., 2008. Functional substitution of the transient membrane-anchor domain in Escherichia coli FtsY with an N-terminal hydrophobic segment of Streptomyces lividans FtsY. *FEMS Microbology Letters*, 287, pp.85–90.

Mandon, E.C., Jiang, Y. & Gilmore, R., 2003. Dual recognition of the ribosome and the signal recognition particle by the SRP receptor during protein targeting to the endoplasmic reticulum. *The Journal of Cell Biology*, 162(4), pp.575–585.

Mary, C. et al., 2010. Residues in SRP9/14 essential for elongation arrest activity of the signal recognition particle define a positively charged functional domain on one side of the protein. *RNA*, 16, pp.969–979.

Mészáros, B., Simon, I. & Dosztányi, Z., 2009. Prediction of Protein Binding Regions in Disordered Proteins. *PLoS Computational Biology*, 5(5).

Meyer, D.I. & Dobberstein, B., 1980. Identification and characterization of a membrane component essential for the translocation of nascent proteins across the membrane of the endoplasmic reticulum. *The Journal of Cell Biology*, 87, pp.503–508.

Miller, J.D. et al., 1995. The beta subunit of the signal recognition particle receptor is a transmembrane GTPase that anchors the alpha subunit, a peripheral membrane GTPase, to the endoplasmic reticulum membrane. *The Journal of Cell Biology*, 128(3), pp.273–282.

Mircheva, M. et al., 2009. Predominant membrane localization is an essential feature of the bacterial signal recognition particle receptor. *BMC Biology*, 7, p.76.

Mohan, A. et al., 2006. Analysis of molecular recognition features (MoRFs). *Journal of*

Molecular Biology, 362, pp.1043–1059.

Murugan, A., Huse, D.A. & Leibler, S., 2012. Speed, dissipation, and error in kinetic proofreading. *Proceedings of the National Academy of Sciences*, 109(30), pp.12034–12039.

Neher, S.B. et al., 2008. SRP RNA controls a conformational switch regulating the SRP-SRP receptor interaction. *Nature Structural & Molecular Biology*, 15(9), pp.916–923.

Noriega, T.R. et al., 2014. Signal recognition particle-ribosome binding is sensitive to nascent chain length. *The Journal of Biological Chemistry*, 289(28), pp.19294–19305.

Notredame, C., Higgins, D.G. & Heringa, J., 2000. T-Coffee: A novel method for fast and accurate multiple sequence alignment. *Journal of Molecular Biology*, 302(1), pp.205–217.

Oldfield, C.J. et al., 2005. Comparing and combining predictors of mostly disordered proteins. *Biochemistry*, 44, pp.1989–2000.

Oldfield, C.J. et al., 2008. Flexible nets: disorder and induced fit in the associations of p53 and 14-3-3 with their partners. *BMC Genomics*, 9.

Oldfield, C.J. & Dunker, A.K., 2014. Intrinsically disordered proteins and intrinsically disordered protein regions. *Annual Review of Biochemistry*, 83, pp.553–584.

Parlitz, R. et al., 2007. Escherichia coli signal recognition particle receptor FtsY contains an essential and autonomous membrane-binding amphipathic helix. *The Journal of Biological Chemistry*, 282(44), pp.32176–32184.

Peluso, P. et al., 2001. Role of SRP RNA in the GTPase cycles of Ffh and FtsY. *Biochemistry*, 40(50), pp.15224–15233.

Powers, T. & Walter, P., 1997. Co-translational protein targeting catalyzed by the Escherichia coli signal recognition particle and its receptor. *The EMBO Journal*, 16(16), pp.4880–4886.

Roy, R., Hohng, S. & Ha, T., 2008. A practical guide to single-molecule FRET. *Nature Methods*, 5(6), pp.507–516.

Seu, K.J. et al., 2007. Effect of surface treatment on diffusion and domain formation in supported lipid bilayers. *Biophysical Journal*, 92(7), pp.2445–2450.

Shan, S., 2016. ATPase and GTPase Tangos Drive Intracellular Protein Transport. *Trends in Biochemical Sciences*, 41(12), pp.1050–1060.

Shan, S., Chandrasekar, S. & Walter, P., 2007. Conformational changes in the GTPase modules of the signal reception particle and its receptor drive initiation of protein translocation. *The Journal of Cell Biology*, 178(4), pp.611–20.

Shan, S., Stroud, R.M. & Walter, P., 2004. Mechanism of Association and Reciprocal Activation of Two GTPases. *PLoS Biology*, 2(10), pp.1572–1581.

Shen, K. et al., 2012. Activated GTPase movement on an RNA scaffold drives co-translational protein targeting. *Nature*, 492(7428), pp.271–275.

Shen, K. & Shan, S., 2010. Transient tether between the SRP RNA and SRP receptor ensures efficient cargo delivery during cotranslational protein targeting. *Proceedings of the National Academy of Sciences*, 107(17), pp.7698–7703.

Shen, K., Zhang, X. & Shan, S., 2011. Synergistic actions between the SRP RNA and translating ribosome allow efficient delivery of the correct cargos during cotranslational protein targeting. *RNA*, 17(5), pp.892–902.

Shepotinovskaya, I. V, Focia, P.J. & Freymann, D.M., 2003. Crystallization of the GMPPCP complex of the NG domains of Thermus aquaticus Ffh and FtsY. *Acta Crystallographica Section D: Biological Crystallography*, 59(10), pp.1834–1837.

Shepotinovskaya, I. V & Freymann, D.M., 2002. Conformational change of the N-domain on formation of the complex between the GTPase domains of Thermus aquaticus Ffh and FtsY. *Biochimica et Biophysica Acta*, 1597(1), pp.107–114.

Stjepanovic, G. et al., 2011. Lipids trigger a conformational switch that regulates signal recognition particle (SRP)-mediated protein targeting. *The Journal of Biological Chemistry*, 286(26), pp.23489–23497.

Thompson, R.C. & Karim, A.M., 1982. The accuracy of protein biosynthesis is limited by its speed: high fidelity selection by ribosomes of aminoacyl-tRNA ternary complexes containing GTP[gamma S]. *Proceedings of the National Academy of Sciences*, 79(16), pp.4922–4926.

Walter, P. & Blobel, G., 1980. Purification of a membrane-associated protein complex required for protein translocation across the endoplasmic reticulum. *Proceedings of the National Academy of Sciences*, 77(12), pp.7112–7116.

Walter, P. & Johnson, A.E., 1994. Signal sequence recognition and protein targeting to the endoplasmic reticulum membrane. *Annual Review of Cell Biology*, 10, pp.87–119.

Ward, J.J. et al., 2004. Prediction and functional analysis of native disorder in proteins from the three kingdoms of life. *Journal of Molecular Biology*, 337(3), pp.635–645.

Weiche, B. et al., 2008. A cleavable N-terminal membrane anchor is involved in membrane binding of the Escherichia coli SRP receptor. *Journal of Molecular Biology*, 377(3), pp.761–773.

Wohlgemuth, I., Pohl, C. & Rodnina, M. V, 2010. Optimization of speed and accuracy of decoding in translation. *The EMBO Journal*, 29(21), pp.3701–3709.

Wright, P.E. & Dyson, J.H., 2015. Intrinsically disordered proteins in cellular signalling

and regulation. *Nature Reviews of Molecular Cell Biology*, 16(1), pp.18–29.

Zelazny, A. et al., 2009. The NG domain of the prokaryotic signal recognition particle receptor, FtsY, is fully functional when fused to an unrelated integral membrane polypeptide. *Proceedings of the National Academy of Sciences*, 94(12), pp.6025–6029.

Zhang, D. & Shan, S., 2012. Translation elongation regulates substrate selection by the signal recognition particle. *The Journal of Biological Chemistry*, 287(10), pp.7652–60.

Zhang, X. et al., 2009. Multiple conformational switches in a GTPase complex control co-translational protein targeting. *Proceedings of the National Academy of Sciences*, 106(6), pp.1754–1759.

Zhang, X. et al., 2010. Sequential checkpoints govern substrate selection during cotranslational protein targeting. *Science*, 328(5979), pp.757–60.

Zhang, X., Kung, S. & Shan, S., 2008. Demonstration of a multistep mechanism for assembly of the SRP x SRP receptor complex: implications for the catalytic role of SRP RNA. *Journal of Molecular Biology*, 381(3), pp.581–93.

Zhang, X. & Shan, S., 2014. Fidelity of Cotranslational Protein Targeting by the Signal Recognition Particle. *Annual Review of Biophysics*, 43, pp.381–408.